Processing of directionally cast nickel-base superalloys: solidification and heat treatments

Jonathan Cormier, Charles-André Gandin

PROCESSING OF DIRECTIONALLY CAST NICKEL BASED SUPERALLOYS – SOLIDIFICATION AND HEAT TREATMENTS

Jonathan CORMIER[1], Charles-André GANDIN[2]

[1] ISAE-ENSMA, Institut Pprime, UPR CNRS 3346, 1 avenue Clément Ader, BP 40102, 86961 Futuroscope-Chasseneuil, France

[2] MINES ParisTech, PSL Research University, CEMEF, UMR CNRS 7635, CS10207, 1 rue Claude DAUNESSE, 06904 Sophia Antipolis, France

Abstract

After presenting the state-of-the-art Bridgman casting process to obtain single crystalline components, as well as alternative directional solidification techniques, common processing defects (recrystallized grains, freckles, microsegregation, slivers …) are reviewed and their formation mechanisms are discussed. The typical heat treatment sequence applied to Ni-based single crystal superalloy (when needed) is then detailed from both microstructure mechanical properties points of view. Creep properties of these alloys are shown to be mainly dependent on the heat treatments following investment casting, especially the solution heat treatment. Conversely, fatigue properties are mainly controlled by the solidification processes, through the casting pore size and spatial distribution, when oxidation has no major contribution to the crack initiation mechanisms.

1) Introduction

The *thermodynamic cycle of gas turbine engines* reveals that better efficiency can be achieved when increasing the operating temperature. This simple rule remains the main driver for designing and engineering parts, which includes the development of materials as well as the processing technologies, both for aero-engines and land-based power generation gas turbines. More precisely, the cold compressed gas entering the combustion chamber must leave it with a maximum temperature when entering the subsequent turbine. The first blading row of the gas turbine, just behind the combustion chamber, thus experiences the highest temperature and pressure. It is certainly the most significant constraint when designing the turbomachinery. Thus, the solutions for these turbine components must withstand very high loads at elevated temperatures, not mentioning the severe gas environments and the long periods of time, all repetitively.

Before the Second World War, at the beginning of the development of gas turbine for aero-engine applications, iron-based cold wrought materials were first used [1]. The superiority of *nickel-based superalloys* was yet very soon recognized, notably for its exceptional creep and fatigue properties at high operating temperature as well as its resistance to oxidation and corrosion [2]. Nickel-based superalloys were first shaped by extrusion and forging. But with always higher strength and the introduction of hollow blade designs, *investment casting* based on the lost-wax process was developed. It is the current processing route for all turbine blades made of nickel-base superalloys, although concurrent methodologies are being investigated based on additive manufacturing [3].

The hollow *design* aims at defining cooling passages for fresh air as well as weight reduction. This major breakthrough in turbine blade engineering started in the 60’s and led to dramatic increase of the turbine entry temperature. It is still a topic of optimization by engine

manufacturers. But the other main innovation over the second half of the twentieth century was due to alloy *elaboration* by metallurgists. With uninterrupted demand for higher mechanical properties at more elevated temperatures, alloy cleanliness was a crucial requirement. This was achieved by introducing multiple successive melting of alloys under vacuum, thus considerably reducing non-metallic inclusions and chemical inhomogeneity and achieving a very high control of composition [1]. Another main step was the constant search for better *compositions* of the nickel-base superalloys. The basic trend consisted in replacing Cr by γ'-forming elements such as Al, Ti and Ta, increasing the γ'-solvus temperature by additions of Ta and W, and finally introducing creep-strengthening elements Re, W, Ta, Mo and Ru [2, 4]. The design of the alloys could then become more systematic by defining automatic procedures that scan the chemical species and its content, access computed properties using thermodynamic and physical databases, and make use of criteria to select compositions [5]. Nowadays, the *microstructure* leading to the highest mechanical properties for turbine blades are directionally solidified *single crystal* (SX) with chosen crystallographic orientation so as to suppress the weakening effects of grain boundaries. The SX components are heat treated to reach around 70% of coherent γ'-precipitates in a γ-matrix phase while maintaining a small lattice misfit, high creep strengthening and oxidation resistant properties. Finally, multilayer coatings are applied to enhance the corrosion and oxidation properties, increasing the durability of these expensive parts when operating at a temperature close to the γ'-solvus temperature in severe gas environments, for long periods of time and thousands of cycles. With typically 10 alloying elements and use of noble and rare chemical species, the SX nickel-based materials are complicated metallic alloys. They challenge our metallurgical and mechanical understanding as most of theoretical studies are developed for simple model alloys, often dilute with only few chemical species.

Historical development of directional solidified SX components made of nickel-based superalloys is a paramount example of how materials properties and processing of products are intimately linked. The present contribution aims at giving the status of the interplays between processing and material properties for SX components. It will start by introducing the general concepts of the casting technologies and the related solidification defects. Modeling efforts will be cited. Heat treatments of as-cast components contributing to define the required (service) mechanical properties are important steps in the processing route. They will thus be introduced and discussed, also focusing on related defects. Conclusions will be drawn on perspectives for further improvements and innovations.

2) Directional solidification and related defects

2.1) Generalities on the casting processes

With the advent of nickel base superalloys for gas turbines, shaping from the liquid has become essential. The reasons are multiple. They include the limitations of machining techniques for complicated hollow geometries due to the design of internal cooling passages for in-service temperatures higher than the compressor-chamber gas temperature. The high strength properties of the superalloys also infer dedicated and expensive tooling for machining. So direct casting of a liquid melt into a mold has quickly become the usual route.

Due to the demand for highly precise geometries, including thin walls with complex shape, the lost-wax casting process was adopted. It starts by making a replica of the desired nickel-base superalloy component by injecting wax around ceramic cores in to a metallic die. Several such wax plus core models are assembled as a cluster by adding gates and runners forming a tree like structure later defining the filling path of the molten metal. Ceramic filters are integrated as part of the gates/runners so as to block large inclusions that may be present in the melt and to reduce melt turbulence. The next step consists of making a ceramic mold. The wax assembly is immersed into slurries of colloidal silica binder and sand-like stuccos. The operation is repeated several times so as to form a thick and rigid coating. The mold is dried and the wax is removed, thus forming the ceramic shell with its embedded ceramic cores. Casting is operated in a vacuum induction melting furnace. This permits thorough control of superheat and composition through elimination of dissolved gases, elements traces and oxides [6]. After casting, the ceramic shell and cores are removed, the gates and runners are cut off so only the metallic component plus cores remain. Cores are eliminated prior to heat treatment (see section 3 of this chapter).

In this section are presented main features and issues related to casting of nickel based superalloy to produce single crystalline turbine blades by the lost-wax process. The latter is of particular importance in the processing route of the material as it defines the initial metallurgical microstructures, i.e. the thermodynamic phases, its amount, crystallography, size, morphology, composition and stresses, as well as defects, all taking part in dictating the subsequent forming steps and final properties of the components.

2.1.1) The Bridgman-Stockbarger casting process

In a conventional lost-wax casting, the liquid metal is poured in a static mold and cooling takes place by heat exchange with the surrounding environment in all directions. As a consequence, heat flow is not directional and the structure is mainly isotropic or consist of columnar and equiaxed grains. Components produced with this static mold technology are named “equiaxed”. In fact, this denomination is somewhat abusive: while copious nucleation

of grains takes place at the mold surface, growth proceeds toward the central part of the casting geometry. Seen from its skin after chemical etching, the casting skin indeed looks like an equiaxed structure while most of the grains grew columnar in a direction opposite to the heat flow and meet at the center part of the geometry [7, 8]. In fact, for such equiaxed component, nucleation at mold surface is induced by application of a special coating at the internal surface of the mold containing an inoculant compound (e.g., cobalt aluminate). This is achieved by adding the compound as part of the first slurry of colloidal silica binder forming the ceramic mold. In order to produce directionally solidified components, both nucleation and growth of the solidifying structure need to be well controlled. Directional solidification of nickel-base superalloys to produce single crystal components was first introduced in the sixties [9]. The schematics of a typical set-up based on the so-called Bridgman-Stockbarger directional solidification process is shown in Figure 1a. It consists of (top) a hot zone and (bottom) a cold zone separated by a baffle, as well as a chill plate on which is located the mold. Unlike conventional lost-wax casting, the mold is no longer static. Initially located in the hot zone, it is dynamically moved downward into the cold zone by withdrawing the chill plate at a rigorously controlled velocity. With the hot/cold zones respectively above/below the melting temperature of the alloy, the solidification front is located in a narrow window close to the baffle and growth of the solid proceeds upward at a velocity roughly equal to the withdrawing rate of the chill plate, v. Note that in principle, the temperature gradient at the position of the growth front, G, can also be adjusted by controlling the temperature of the hot zone. Thus both the velocity and the temperature gradient could be controlled, which are the main processing parameters for casting (the cooling rate $\dot{T}$ is simply the product of the last-two parameters when a steady regime is established as $\dot{T} = -G^* v$).

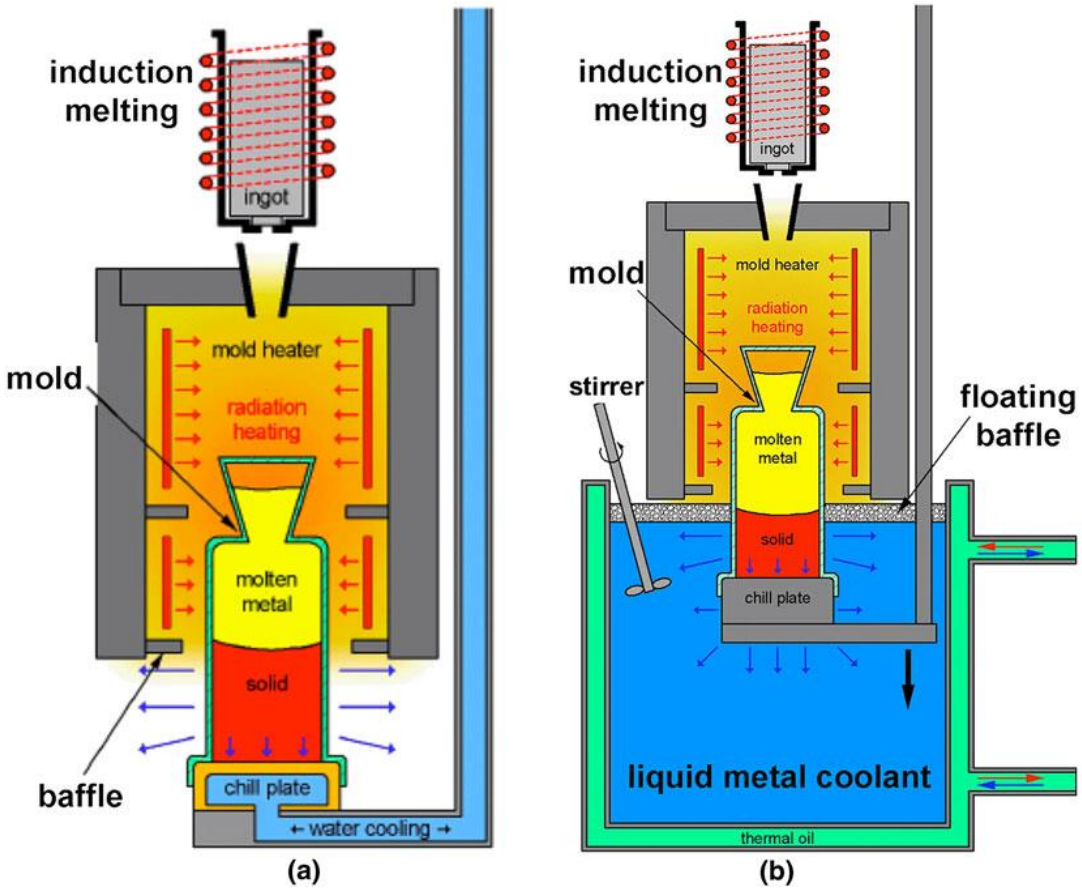

Figure 1 – Schematics of (a) the Bridgman-Stockbarger process and (b) the liquid metal cooling process for directional solidification of nickel base superalloy to produce single crystal turbine blades [10, 11].

As a result of directional solidification, a columnar dendritic microstructure is growing into the melt. For single crystal Ni-based superalloys, they consist of a solid disordered fcc-phase. Its characteristic length scales after complete solidification are the primary dendrite arm spacing, λ_1, and the secondary dendrite arm spacing, λ_2. According to simple literature models [12], they depend on the processing parameters as:

$$\lambda_1 \propto G^{-1/2} \cdot v^{-1/4} \tag{1}$$

$$\lambda_2 \propto G^{-1/3} \cdot v^{-1/3} \tag{2}$$

While derivation of the first relation involves a dendrite tip kinetics theory, the second relation is linked to the physics of coarsening taking place in the mixture region of liquid and solid phases called mushy zone. The latter region is approximately defined by the solidification interval, i.e. the difference between liquidus temperature, T_L, at which the first solid phase forms from the melt and the solidus temperature, T_S, at which the last liquid solidifies. Such relations are approximate and dependencies with alloying elements are not given. More detailed experimental studies and relationship coming from direct measurements

for nickel-based superalloys are available [13]. Although compositions of single crystal Ni-based superalloys are defined to avoid the formation of secondary interdendritic phases formed in the residual liquid located at the end of the mushy zone, formation of peritectic and/or eutectic microstructures could happen, involving an ordered fcc-phase. The solidification structure thus generally consists of a primary dendritic disordered fcc-phase and a mixture of secondary disordered and ordered fcc-phases, as will be further described in the present contribution. Another feature of the as-cast microstructure includes microporosity. It is naturally presents as its origin is related to the density variations between phases in the mushy zone. Directional solidification is well suited to reduce it but its full elimination could be challenging.

Another important feature of a single crystalline microstructure is the crystallographic orientation. Its selection requires using either a solid seed or/and a grain selector. In the first configuration, the seed is a single crystal with controlled orientation, positioned between the chill plate and the component, with one of its <100> directions aligned with a chosen component axis. For instance, considering a turbine blade, its main airfoil axis (along its height) is chosen to host a <100> crystallographic direction by positioning the seed accordingly. Partial remelting of the seed takes after the liquid is poured in the ceramic mold and epitaxial growth proceeds, propagating the crystal orientation through the entire component. Note that in nickel-based alloys, the preferred growth directions defined by the trunks and arms of the dendritic microstructure correspond to the <100> crystallographic directions. Thus, a <100> crystal orientation is chosen to correspond to the airfoil direction, usually the normal to the chill plate and thus the direction of the temperature gradient defined by the hot and cold zones of the furnace. It is also worth noting that the secondary <100> directions, the dendrite arms perpendicular to the trunk and main airfoil axis, can also be chosen to correspond to selected component directions. The second configuration makes use of a grain selector. It consists of a constriction designed as part of the ceramic mold from the wax assembly located between the chill plate and the component. Its role is to select a given single crystal orientation from a polycrystalline columnar grain structure arising from randomly nucleated grains in contact with the chill plate. The grain selector geometry can be a simple helix (the so-called “pig tail”), as schematized in Figure 2, or it can take more sophisticated shapes. In any case, its development is based on the fact that the preferred growth direction of the columnar dendritic grains follows a <100> crystallographic direction more or less aligned with the temperature gradient.

2.1.2) Alternate casting processes

While the Bridgman-Stockbarger directional solidification process is by far the most commonly used for the production of nickel-base superalloy single crystal components,

alternate methods have been proposed. Considering that a non-static mold and the presence of hot and cold zones separated by a baffle was a somewhat complex casting process relying on heavy investments, Walser et al. proposed to rely on existing conventional vacuum casting equipment for static molds, still using a chill plate to ensure directional heat flow [14, 15]. This main idea was to optimize cooling from the chill plate and insulation of the ceramic shell using layers of blanket materials. Despite its interest, the so-called SMCT-process was not widely adopted. In fact, upon directional growth of a mushy zone from a chill, the temperature gradient at the dendritic growth front progressively decreases while the velocity increases [16]. In such conditions, the microstructure length scales (Eqs 1-2) can hardly be controlled and, upon low values of the ratio (G / v), nucleation of equiaxed grains takes place, obviously breaking the condition for single crystal growth [17].

The need for higher temperature gradient and velocity was very soon identified. Not only it produces finer microstructures but we also shall see in Session 2.2 its roles on various defects that could happen during solidification. This is why other cooling media were proposed. Figure 1b gives an illustration of the liquid metal cooling process [10, 11, 18]. The cold zone is made of a low melting and low vapor pressure liquid metal (e.g., Sn), maintained at a temperature always much lower than the solidus temperature of the nickel-based superalloy. The ceramic mold filled with the superalloy is thus progressively immersed into the liquid metal. Both the combination of the heat flow through the liquid metal and a baffle floating above it ensures a temperature gradient at the solidification front 2 to 3 times higher compared to the standard Bridgman-Stockbarger casting process in the 1500°C-900°C temperature range. This also offers the possibility to increase the withdrawal rate while maintaining a constant (G / v) ratio, thus increasing productivity. It is worth noticing that a seed is preferred to define the single crystal orientation as using a grain selector implies direct contact of the superalloy melt with the chill plate and risk of mixture with the liquid metal bath. Interaction of the nickel-base superalloy with the liquid metal is also an issue. A variant was thus introduced where the liquid medium is replaced by solid particles (e.g., carbon balls) held in suspension and transported by a continuous flow of inert gas (e.g., argon) [10, 19, 20]. All these processes with higher solidification rates are also known to produce alloys with a smaller casting pore size, and hence better fatigue properties (see last sub-section of this chapter) [10, 11, 21, 22].

Other parameters and manufacturing processing are being considered. One could cite additive manufacturing of single crystal superalloys [3]. Using electron beam, advantages include an even finer microstructure due to always higher temperature gradients, more homogeneous chemical composition and reduced shrinkage porosity compared to investment casting, while recrystallization is an issue if heat treatment is still to be considered. Magnetic field is another direction being investigated for improvement of the superalloy

microstructure [23]. These researches can be considered as new directions for potential breakdown technologies.

2.2) Casting defects

The features identified as defects in the production of single crystal components are numerous and have very diverse origins. Fig. 2 is a classical schematic that reports microstructure related defects observed upon inspection of a turbine blade component after casting. We shall only consider such defects that are directly related to solidification issues, meaning that inclusions, surface scales, critical dimensions and tolerances, and other defects due to non-well controlled foundry practices and/or quality issues with the core, shell and superalloy materials are not considered hereafter.

2.2.1) Crystal structure

There are several origins for the breakdown of the single crystalline structure. When nucleation proceeds on the chill plate, crystal orientation is random and copious. Dendritic growth starts from each nucleus. It requires undercooling, i.e. a driving force identified by the temperature difference between liquidus temperature of the alloy given by thermodynamic equilibrium and the dendrite tip temperature. This undercooling is due to several contributions, including solute diffusion of chemical species segregated at the solid-liquid interface [12, 17]. Because the liquid is undercooled, nucleation of new grains could further happen in the melt in front of the columnar dendrites. In the absence of nucleation, a columnar grain structure grows in the starter block shown in Fig. 2. The growth front is then composed of several grains, each grain containing several dendrite trunks with the same crystal orientation, all dendrite tips at some undercooling, i.e. on an isotherm surface lower than the liquidus temperature of the alloy and perpendicular to the chill plate if one assumes a vertical temperature gradient opposite to the heat flow. The grain density decreases upon growth as only the grains with a <100> dendrite trunk direction well aligned with the temperature gradient survive, giving birth to a fiber texture [24-26]. At the exit of the starter block, i.e. at the entry of the grain selector, there still exist many grains.

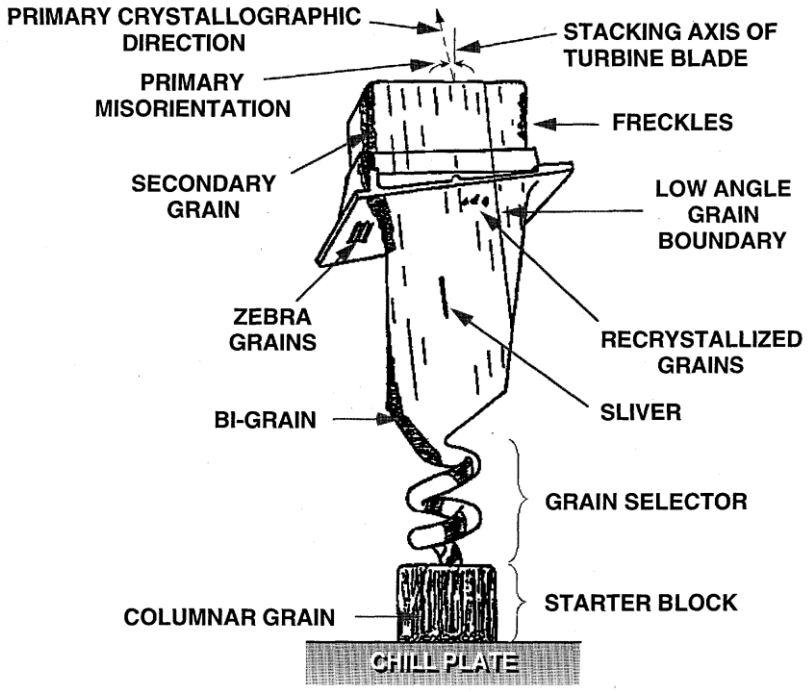

Figure 2 – Schematics of casting defects in a turbine blade [27].

Primary misorientation. The helix geometry aims at selecting a single crystal. It acts as a heat flow channel, where the direction of the temperature gradient basically follows the metal path during cooling. This is due to the insulating role of the ceramic shell, the difference in thermal properties between the mold and the superalloy, as well as cooling from the underneath chill plate [28]. As a consequence of growth competition between secondary branches also propagating the <100> directions of the grains, only a single grain and hence a single crystal orientation remains at the exit of the grain selector. Not only a single crystal must be selected at the exit of the grain selector but also its primary crystallographic direction defined by the direction of the primary dendrite trunks with respect to the stacking axis of the turbine blade. In Fig. 2, the primary misorientation is used to define the possible deviation with the desired crystal orientation. In principle, simulation of dendritic growth can be directly carried out using various methodologies. The Phase Field (PF) method and the Cellular Automaton (CA) methods are the actual two extremes in terms of objectives and scales. While PF is able to directly produce complicated dendritic patterns, CA only aims at propagating grain envelopes. Consequently, PF is much more demanding in terms of computer resources and cannot assess simulation for a whole grain selector. This was yet achieved long time ago by the CA method [29] and is still used for optimization of both the starter block and the grain selector [30, 31]. Nowadays, PF and CA were demonstrated to converge towards satisfying results when considering growth competition of bi-grains, yet limited to binary dilute alloys [25].

Bi-grain, secondary grain and high-angle grain boundaries. As suggested in Fig. 2, it could also happen that the grain selector does not work properly so a bi-grain or more grains survive the growth competition in the helix geometry and propagate in the turbine blade. In this situation, a single crystal may never have been present in the helix. This situation may happen when the heat flow is not well controlled, the helix geometry is not well designed, or if heterogeneous nucleation takes place in the undercooled region ahead of the dendrite tip or in a cold part of the grain selector. Adjectives spurious or stray are used for several types of crystal defects, including undesired grains due to nucleation. It is worth noting that such grains are often seen in large section changes, for instance when leaving the airfoil to enter the platform of a turbine foot geometry (top-left regions in Fig. 2). Simple explanations with observations and analytical models were provided [32, 33]. They involve the time required for the dendritic growth front to propagate in the platform, thus increasing the total undercooling of the liquid together with the risk for spurious nucleation. These spurious grains are often large and with random crystallographic orientation.

Zebra grains. This defect is, again, a region of the component with crystal orientations that differ from the desired single crystal. Their appearance is not similar to secondary grains. Zebra grains are surrounded by the single crystal, they are of limited size and can be made of several distinct crystal orientations. In case of zebra grains located in the platform of Fig. 2, they form as a result of partial remelting of the dendritic structure after its propagation in the undercooled region of the platform [34, 35]. In fact, upon growth of the single crystal, recalescence can take place when the temperature gradient could not be maintained directional and high enough to evacuate the latent heat. Partial remelting leads to detachment of dendrite arms and rotations in the liquid create new crystal orientations. The occurrence of such recalescence can also be modeled when coupling the CA model with heat flow [36].

2.2.2) Microstructure and microsegregation

Solidification is accompanied by segregation: solute species are redistributed between the phases present in the mushy zone. In case of no phase transport by convection, the evolution of the solute composition in all phases leads to the so-called microsegregation. The path of the interfacial compositions upon cooling and solidification, even if it follows thermodynamic equilibrium, can be very complicated as full equilibrium does not necessarily take place. Figure 3 presents a typical microstructure for the single crystal nickel-based superalloy AM1. Its composition can be read in Table 1. Full equilibrium using only thermodynamic data concludes that full γ-phase solidification takes place. This is obviously not the case as γ'-phase is present as part of an interdendritic eutectic microstructure.

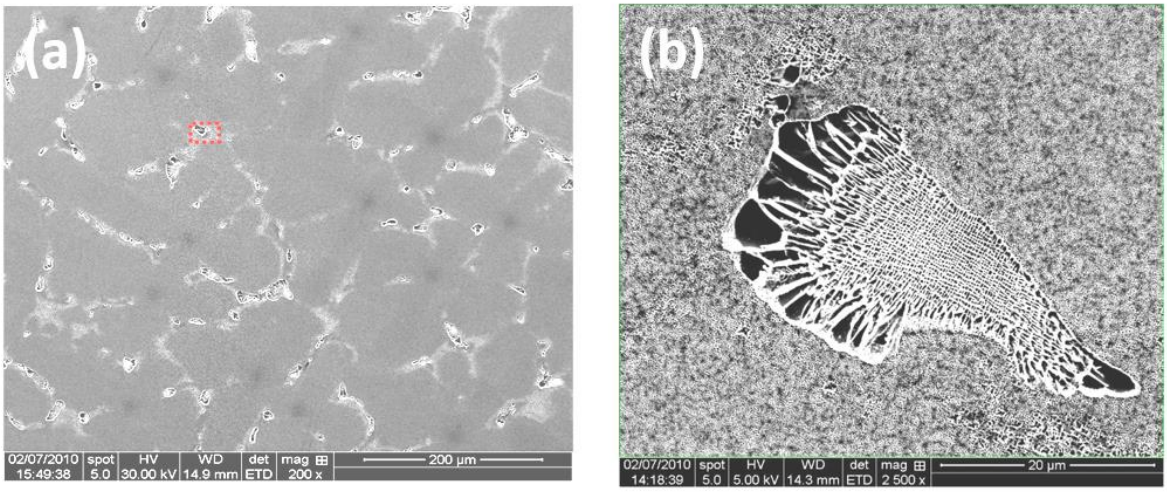

Figure 3 – As-cast microstructure of directionally solidified nickel base superalloy AM1 as observed by electron microscopy revealing (a) primary γ-phase dendritic solidification and (b) an interdendritic eutectic region made of a mixture of the γ- and γ'-phases [Ham09].

Alloy/Element	Ni	Al	Ti	Ta	W	Cr	Co	Mo	Re	Nb	Hf
AM1	Bal.	5.3	1.2	8.0	5.7	7.8	6.5	2.0	/	/	0.05
AM3	Bal.	6.0	2.0	3.5	5.0	8.0	5.5	2.2	/	/	/
MC2	Bal.	5.0	1.5	6.0	8.0	8.0	5.0	2.0	/	/	/
CMSX-4	Bal.	5.6	1.1	6.5	6.4	6.5	9.7	0.6	3.0	/	0.1
CMSX-4 Plus	Bal.	5.7	0.9	8.0	6.0	3.5	10.0	0.6	4.8	/	0.1
CMSX-10K	Bal.	5.7	0.2	8.2	5.5	2.2	3.3	0.4	6.3	0.1	0.03
Quaternary (Fig. 4)	Bal.	5.8	/	7.94	8.84	8.98	/	/	/	/	/

Table 1 – Chemical composition (in wt. pct.) of nickel-based superalloys cited in this contribution.

In practice, the microsegregation path is a consequence of diffusion kinetics and interfacial equilibrium at the γ/l-interface. Explanations involve limited diffusion in the γ-phase while the l-phase can be assumed to be in complete mixing or of uniform composition. This is due to the ratio of the diffusion coefficients for the chemical specie i in phase γ and the D_i^{γ}/D_i^{l} ratio easily reaching 10^{-3}. Consideration of diffusion in the solid with cross diffusion terms is also necessary for nickel-base superalloys. This could be handled with

advanced PF models [37]. Figure 4 presents typical distribution of four chemical species in a quaternary nickel-base superalloy. As can be seen, because the dendritic microstructure is due to γ-phase solidification, it inherits from the solubility of chemical species in the γ-phase. This property is given by the segregation coefficients, i.e. the ratio of the γ-phase composition over the liquid composition at the interface. As stated above, assuming thermodynamic equilibrium at the interface, it can be directly read from the phase diagram. In practice, the CALPHAD method has become a standard for determining these coefficients, although it relies on databases that are mostly fitted from experimental data. In the case reported in Fig. 4, measurements of composition reveal an Al-, Cr- and Ta-depleted and W-enriched dendrite, as well as non-uniform distributions in the dendrite. Also small secondary solidified regions are seen with clear composition differences, here only representing around 1% in volume. Of course, the reported behavior for the solute species in the dendrite is retrieved with Al-, Cr- and Ta-enriched and W-depleted secondary solidified regions.

As-cast microstructure and microsegregation are essential outputs of the lost-wax casting process of nickel-base superalloys. As the eutectic is not generally desired, it could be seen as a defect, similarly as non-uniform chemical compositions in the solidified γ-phase. We shall see later the role of heat treatments for the control of the microstructure and microsegregation.

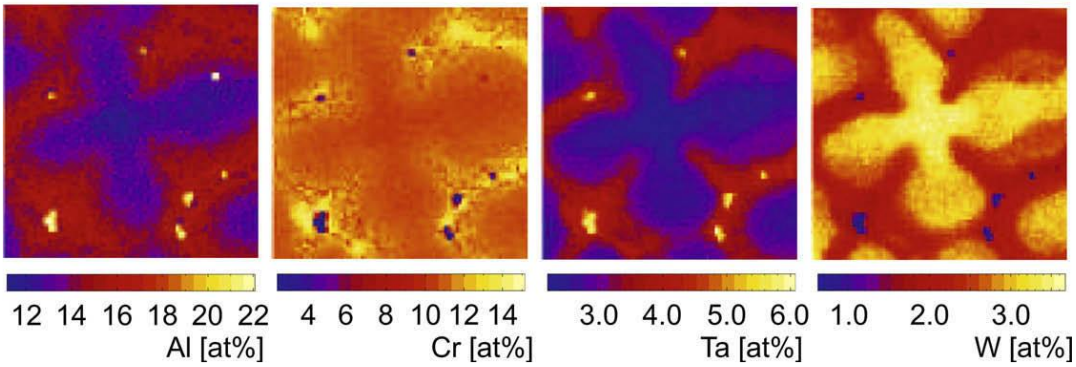

Figure 4 – Distribution of Al, Cr, Ta and W between the dendritic γ-phase and the interdendritic region after directional solidification of the nickel base superalloy (in wt. pct.| in at. pct.) Ni – 5.8|13.06 Al – 8.98|10.49 Cr – 7.94|2.67 Ta – 8.84|2.92 W as measured by wavelength dispersive X-ray spectroscopy [37]. Processing conditions: temperature gradient $G = 20.0\ K.mm^{-1}$ and withdrawal rate $v = 5\ mm.min^{-1}$.

2.2.3) Freckles

Freckles defects are shown in Figure 5. They appear as chains of small equiaxed grains in the turbine airfoil of Fig. 5a where variations of grey colors compared to the rest of the

geometry clearly reveal different crystallographic orientations. Their origin is the redistribution of chemical species by liquid transport. During solidification, due to microsegregation, the interdendritic liquid regions are enriched or depleted as a result of solidification and interfacial equilibrium (see explanation in Section 2.2.2). Variations in the liquid composition induce buoyancy forces due to inhomogeneous density. In case of density inversion close to the dendritic growth front, liquid can flow upward, leave the mushy zone and accumulate in the liquid melt, thus creating segregation at the scale of the product, named macrosegregation. The transport of solute and its effect on dendritic growth are illustrated in Figure 6 where the first in-situ real-time X-ray radiography of plumes of solute ahead of a columnar dendritic growth front observed in the 2nd generation CMSX-4 (see composition in Table 1) nickel-based SX superalloy were observed (variations of the grey level in the liquid region) [38]. These observations also reveal the strong interaction between the flow of solute and the growth front. Following the dendrite tip identified by the white arrow (Fig. 6a) with time, one can draw its position (Fig. 6b), velocity (Fig. 6c) and above liquid composition qualitatively given by the grey level (Fig. 6d). The latter information reveals a periodic oscillation due to the propagation of solute convection cells shown in Fig. 6a. The correlation with the growth velocity evolution is immediate when considering the vertical dashed lines: the times at maximum grey level correspond to the time at minimum velocity and oscillation of the growth front propagation. Of course, this is in link with the main contribution for dendritic growth, previously referred to as the solutal undercooling. When the intensity of the grey level increases, the average supersaturation decreases and so does the velocity. Although not reported in this figure, it could be seen that each dendrite has an oscillation regime that travel with the solute plumes, i.e. not only upward but also from right to left due to a larger convection cell in the above melt. On the right-hand-side of the mushy zone, in contact with the border of the sample, is a larger channel that is progressively forming. Closer look shows that this channel is the origin of a higher upward solute flow. Later on, it solidified with equiaxed grains formed by fragmentation of the existing dendritic microstructure and/or nucleation in the liquid channel [38], giving rise to a freckle.

Several criteria have been proposed in the literature for the formation of the freckles. The simplest considered the effect of the processing parameters previously introduced [39]. Freckles appear when the product $G^{-m} \cdot v^{-n}$ becomes too low, where m and n are positive values lower than unity. Note that such relation is comparable to Eq. 1-2 and correspond to the observations that a critical value of the primary spacing exist above which freckles form. This observation is nothing but the manifestation of the mushy zone permeability, directly proportional to the microstructure length scale. The larger the dendrite arm spacing, the larger the permeability, thus permitting circulation of a convective flow into the mushy zone and transport of solutal species above the dendritic growth front. An experimental correlation was later derived based on a large experimental database with systematic characterization of the

primary dendrite arm spacing, the liquid density variation due to segregation and the solidification interval [40]. Finally, Rayleigh-type criteria were proposed, where the influence of fluid flow was estimated [41, 42]. In principle, such criteria are better suited as they compare buoyancy forces to the friction forces in presence of a mushy zone. So properties including liquid viscosity, mushy zone permeability and thus microstructure length scale and solidification path, liquid density variations with composition and temperature, as well as heat diffusion, all these parameters could be included. In practice, however, properties are often not very well established and the role of the solidifying geometry is difficult to account for. This is why efforts continue to account for more physics in direct simulations of thermo-solutal convection, i.e. the interaction of the solidifying microstructure with liquid flow [43].

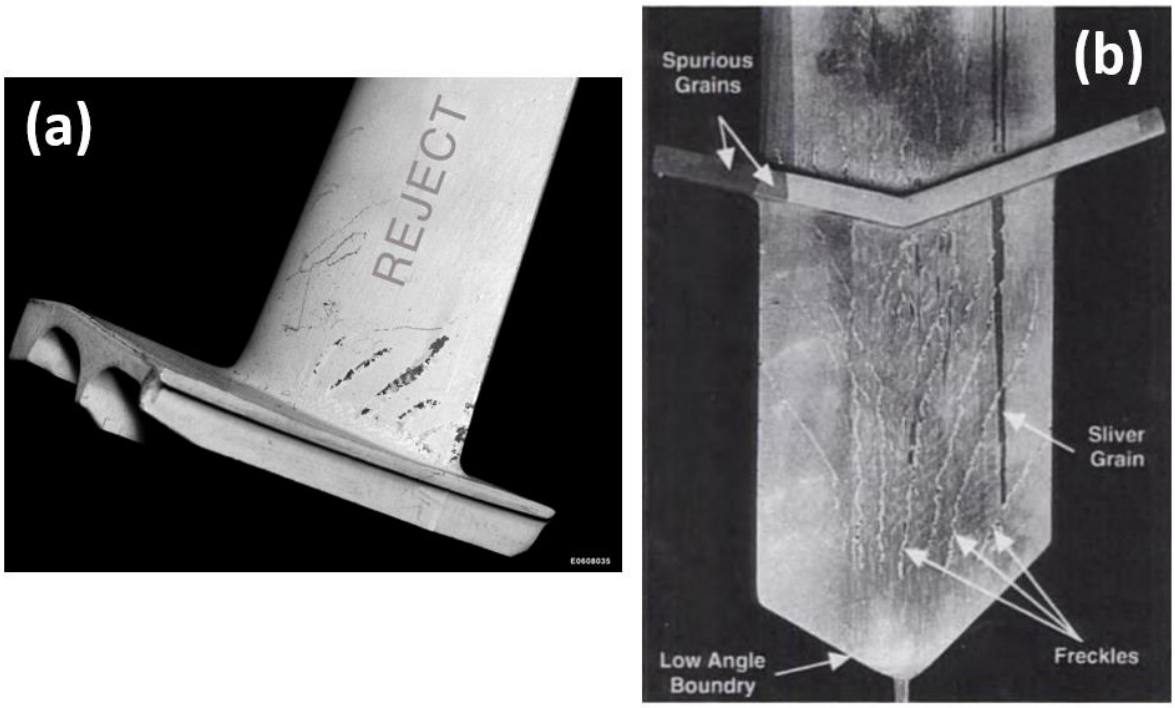

Figure 5 – Examples of the freckles defect formed upon directional solidification of (a) a turbine blade geometry and (b) a dummy geometry also exhibiting spurious grains, low angle grain boundaries and sliver grains [44].

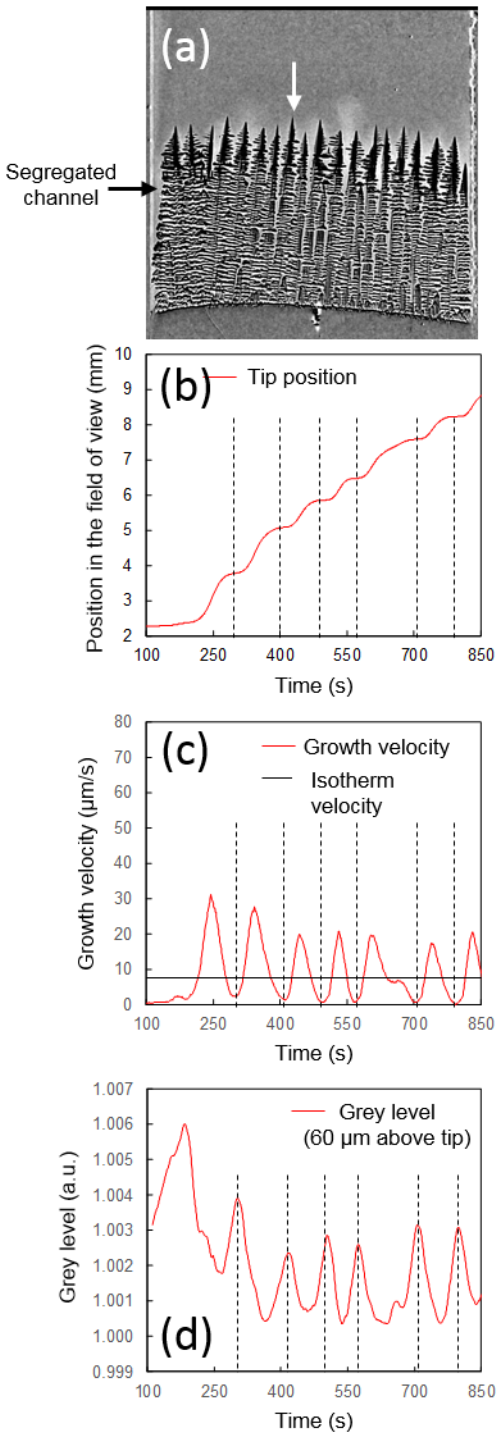

Figure 6 – Experimental analyses of a directionally solidified CMSX-4 superalloy sample processed with in situ and in real-time observations by means of synchrotron X-radiography at the European Synchrotron Radiation Facility (ESRF, Grenoble, France). Temperature gradient G = 44 K.cm^{-1}, growth rate v = 7.5 µm.s^{-1} [38].

2.2.4) Deformation related defects

Slivers and low angle grain boundaries. An example of a sliver grain is show in Fig. 5. While its primary <100> dendrite trunk direction only slightly differs from the surrounding single crystal, the other <100> directions could be more misoriented. This means that a rotation has taken place about the primary <100> direction. The literature proposes various origins for this defect. However, the most recent explanations suggest that deformation of the growing dendritic microstructure could be the best explanation [45]. In fact, thanks to tremendous progress made by direct observations of phase transformations using in-situ real-time X-ray radiography, the deformation can now be imaged in metallic alloys [46]. Direct correlation was thus possible between deformation and rotation of sliver-type defects. In fact, the role of thermo-mechanical stresses built with solid state precipitation of the ordered γ' phase in the primary dendritic disordered γ phase below the solidus temperature was soon identified to explain cumulated deformation and low angle grain boundaries also referred to as sub-grains, shown in Fig. 5 [47].

Recrystallized grains. This defect is built during cooling of the metal trapped between the ceramic parts, i.e. the core and the shell of mold. All three materials have different dilatation coefficients. Upon cooling, the thermo-mechanical histories are thus different, leading to the build-up of stresses in the metal. These stresses are at the origin of the nucleation and growth of recrystallized grains during later heat treatments. Figure 7 presents recrystallized grains as observed in the airfoil of a component designed to be a single crystal. The abrupt color changes reveal the presence of several grains, i.e. variations of the crystallographic orientations. The part not being a single crystal must simply be discarded, decreasing the yield rate of the production route. Formation of recrystallized grains following single crystal casting has only been recently studied. Deformations were first imposed by indentation at room temperature of single crystal samples. A minimum value of the plastic strain was identified above which recrystallization takes place during the solution heat treatment, e.g. typically 6 hours at 1315 °C in case of CMSX-4 alloy [48]. But compressive and tensile tests were also tested at several temperatures, followed by isothermal annealing heat treatments for various parameters (holding time and duration) [48-50]. The presence of recrystallized grains is found to depend on *i*- the plastic strain, *ii*- the annealing temperature, and *iii*- the temperature at which the specimens were deformed. Most of the experiments are conducted with plastic strains of 4% [48, 50] and of 5% [49] when the annealing temperature and the deformation temperature are studied. But depending on the plastic strain, the annealing temperature seems to influence the formation of recrystallized grains. Similarly for CMSX-4, if the temperature at which 4% plastic strain is introduced is lower than 950 °C, no recrystallized grains were formed for annealing treatments below 1260 °C [50]. Finally, the recrystallized area is a direct function of the annealing temperature. Above the solvus of the γ' precipitates in the γ matrix phase (around 1300 °C), the recrystallized area increases rapidly.

Below this temperature it would be a direct function of the fraction of γ' precipitates. Despite these observations and electron microscopy investigations, author's explanations do not converge to explain the recrystallization mechanisms [49]. A special feature of the recrystallized grains is that they are not immediately detectable in the as-cast state. They develop during the heat treatments that follow casting which will be the object of the next section.

Figure 7 – Recrystallized grains in the airfoil of a component designed as a single crystal.

3) Heat treatments and microstructure optimizations

3.1) Generalities on heat treatments

Solution and aging heat treatments (see schematic illustration in Fig. 8) are usually applied to most of the single crystalline components (i.e. blades and vanes) for which a given level of mechanical properties in creep and fatigue is expected. It has to be noted that several components may be used in as-cast state (e.g. vanes or shrouds) to reduce production costs and/or to limit the development of defects during processing, such as recrystallization (Fig. 10b). During production of SX components, typical heat treatments are composed of a solution heat treatment and of two aging heat treatments at least (see Fig. 8). Moreover, other operations (de-sulfurization, de-oxidation, pre-oxidation of the bond-coat before top-coat deposition…) lead to additional temperature cycles of the components before being serviced. In the following of this chapter, we will mainly focus on key heat treatments steps controlling the microstructure and mechanical properties of SX alloys, namely, the solution heat treatment and agings.

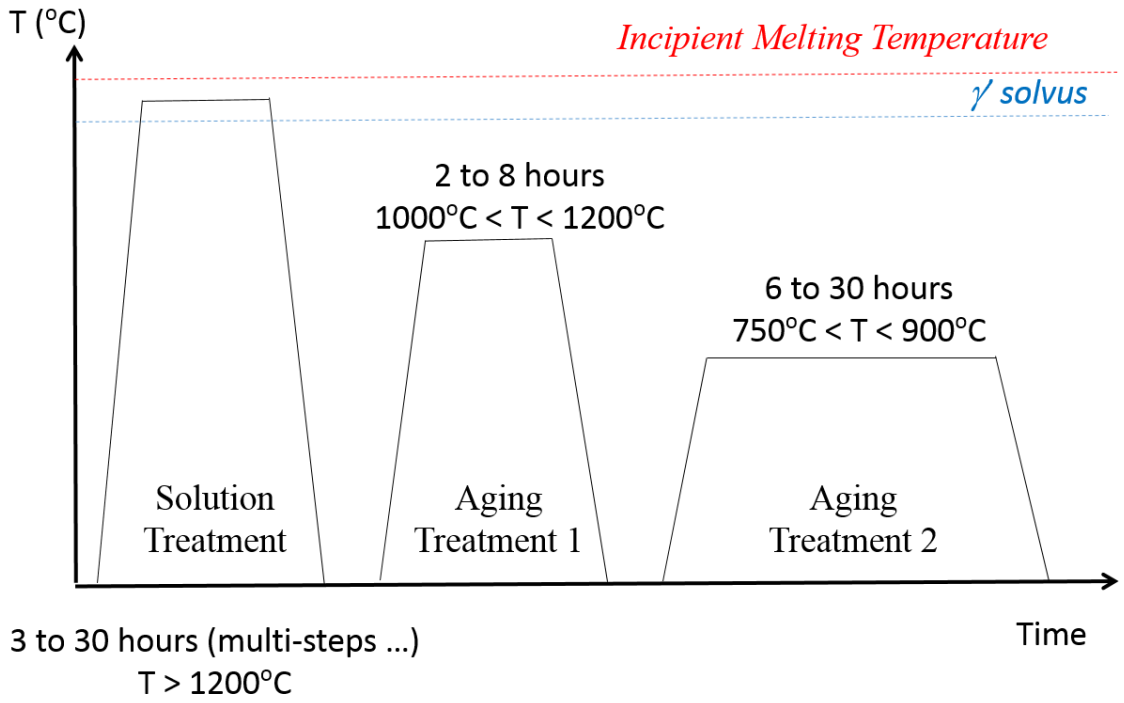

Fig. 8 – Typical heat treatments schedule

Typical metallurgical defects that can be encountered/should be avoided in SX components are presented in Figs. 9 and 10. Casting pores are shown in Fig. 9a in the case of MC2 (see composition in Table 1) 1st generation SX alloy whose solidification process was

done with issues in withdrawal rate. These casting pores are forming in the interdendritic spacings during the dendritic growth in the last stages of solidification of the mushy zone [51-54]. These pores can reach a size of up to 100-150 µm, depending on the casting parameters and alloy's chemistry [22, 55, 56]. It will be shown in the last sub-section of this chapter how these pores are critical in controlling fatigue properties if no Hot Isostatic Pressing (HIP) is applied. In Figs 9b and 10a, typical microstructures of γ/γ' eutectics and local incipient melting are presented, respectively. Finally, new grains nucleated at the surface of a component profile after solution heat treatment due to, e.g., a local surface plasticization during shell removal or local residual stresses introduced during the solidification are shown in Fig. 10b. The authors will refer to these figures in the following when referring to such typical metallurgical defects.

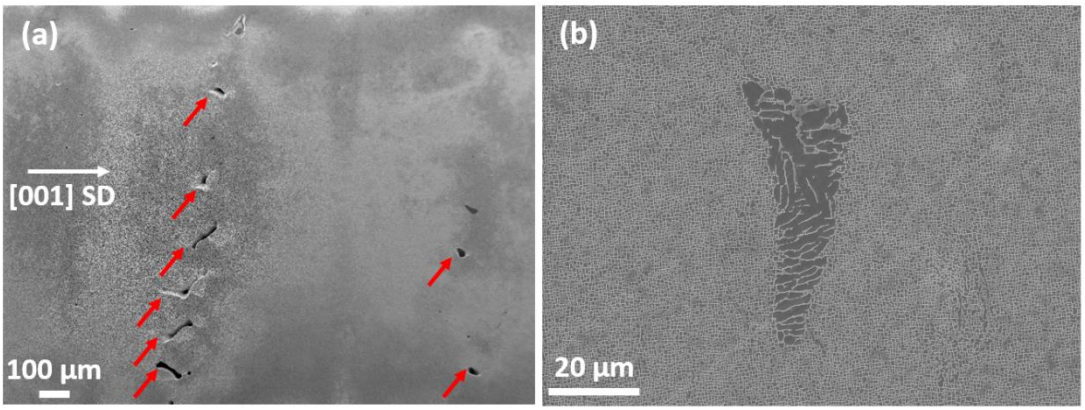

Fig. 9 – Typical metallurgical defects that can be encountered in SX components after investment casting: (a) casting pores (see red arrows) and (b) γ/γ′ eutectic pool. The nearly [001] solidification direction (SD) is indicated by a white arrow in (a). (authors own works)

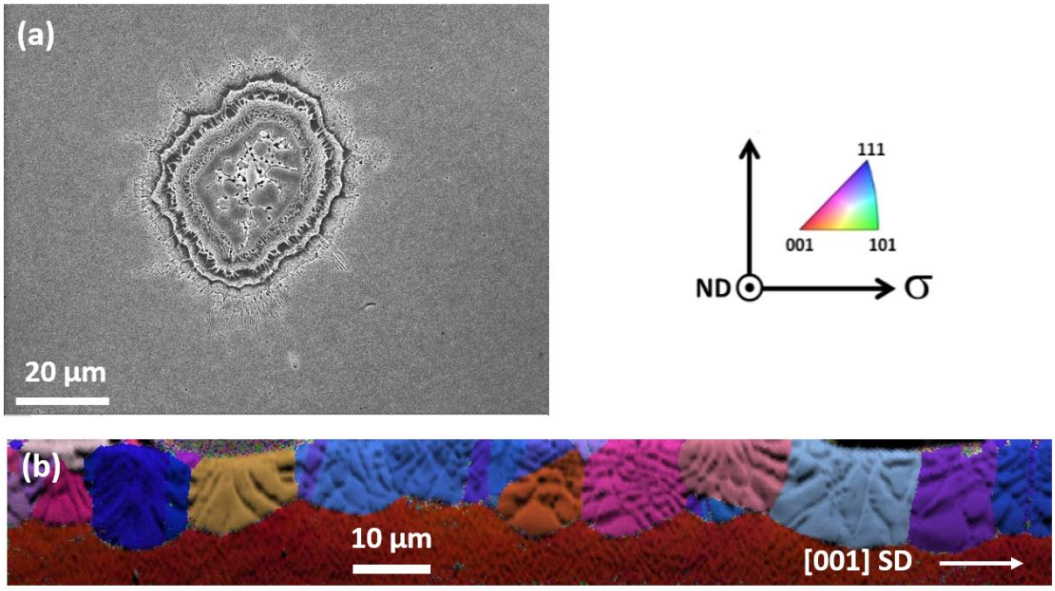

Fig. 10 – Typical metallurgical defects that can be encountered in SX components after solution heat treatment: (a) incipient melting in interdendritic spacings and (b) surface recrystallization due to local surface plasticization. The nearly [001] solidification direction (SD) is indicated by a white arrow in (b). (authors own works)

3.1.1) Solution heat treatment

The main objective of solution heat treatments (SHT) is to break the dendritic chemical inhomogeneity inherited from the solidification and to dissolve the γ/γ' eutectics pools [57]. For this, the alloy is usually heated above the γ' solvus temperature and the closest possible to the incipient melting temperature (or solidus) to achieve the best chemical homogeneity in a reduced time (see Fig. 8). Typical SHT are either performed in a stepwise manner (see Fig. 11a) or using a fixed heating ramp (see Fig. 11b) or a combination of both. These stepwise or ramped SHT procedures are especially mandatory for alloys with a high amount of refractory elements (typically, for 2nd, 3rd and 4th generation SX alloys with more than 3.0 wt. pct. Re containing alloys) since a progressive chemical homogenization will be achieved with each temperature increment meanwhile increasing progressively the incipient melting temperature [58-60]. These progressive (stepwise) increases in temperature during SHT as presented in Fig. 11a are also more convenient in industrial heat treatment furnaces to ensure almost similar temperature profiles for each component treated in a same batch.

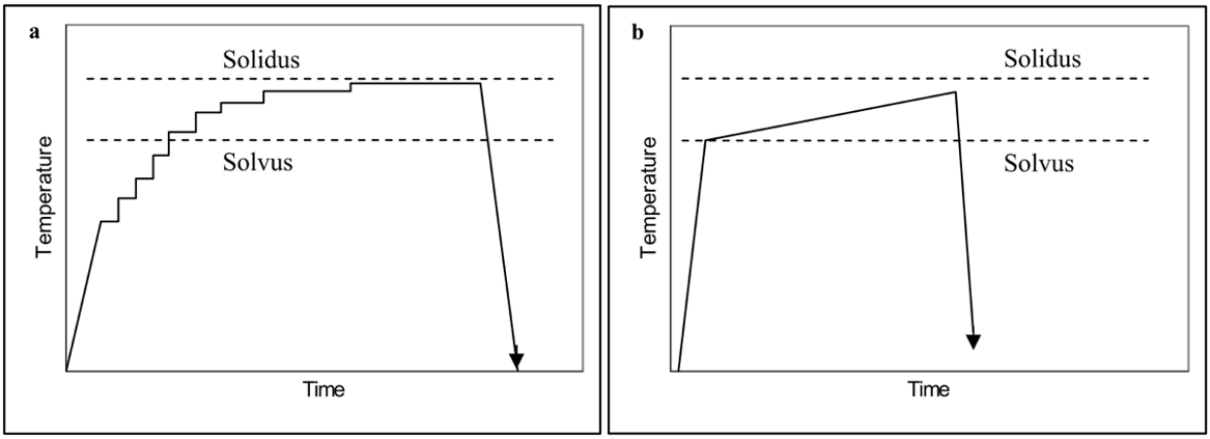

Fig. 11 – Traditional step-wise (a) and ramp (b) solution heat treatments. Adapted from [61].

In principal, a SHT is considered to be optimal when almost all γ/γ' eutectics pools have been dissolved, as illustrated in Fig. 12 in case of CMSX-4 Plus alloy (see composition in Table 1), and when the γ' precipitate size distribution is homogeneous across the dendritic structure, as shown in Figs. 13e and 93f. In fact, when a residual chemical micro-segregation is still present, mainly in heavy elements such as Re, W and Mo, the γ' precipitate size distribution is inhomogeneous across the dendritic structure, with coarser precipitates and a higher volume fraction of γ' phase within interdendritic spacings as compared to primary dendrite arms (compare Fig. 93b and 93c). Such a difference in precipitate size is known to degrade tensile and creep strengths of the alloy in a wide temperature range according to pioneering works of Caron and Khan [62-64]. Finally, limiting or ideally suppressing γ/γ' eutectics pools is highly desirable from a creep strength point of view. Indeed, the lower the γ/γ' eutectics pools fraction will be, the higher the fraction of efficient fine γ' precipitates as the ones presented in Figs. 93e and 93f, overall improving creep strength [65]. It has however been shown in a recent study of L.M. Bortoluci Ormastroni et al. that a non-negligible fraction of γ/γ' eutectics pools can be kept without inducing a debit in creep, tensile and fatigue properties [56]. Another very important part of the SHT is the final cooling before subsequent agings. The impact of this final cooling on microstructure and mechanical properties will be presented in a forthcoming sub-section of this chapter. If the main aim of the SHT consist in optimizing bulk microstructure precipitation through elemental chemical interdiffusion across the cast dendritic structure, one should also mention that achieving a good chemical homogeneity is also required to further limit/suppress the development of secondary reaction zone (SRZ) during the bond coat deposition process in 2nd, 3rd and 4th generation SX alloys [66] and to improve their oxidation/corrosion resistance [67, 68]. Finally, the SHT also leads to the nucleation of so-called “homogenization” pores in interdendritic spacings due to the imbalance of diffusing elements across the dendritic structure, in addition to the growth of solidification pores [53, 54, 69]. These homogenization

pores being far smaller (typical size of ~ 10-20 µm) than solidification pores, they do not have any noticeable impact on the mechanical properties [70].

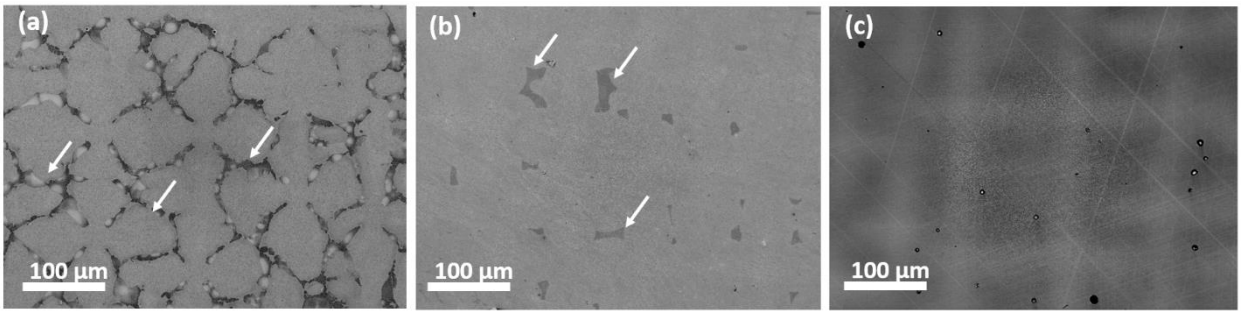

Fig. 12 – Evolution of the γ/γ′ eutectic pools (see white arrows) as a function of the applied solution treatment in 3rd generation CMSX-4 Plus SX alloy: as-cast structure (a), after a ST of 15h at 1330°C (b) and after 15h at 1340°C (c). Adapted from [56].

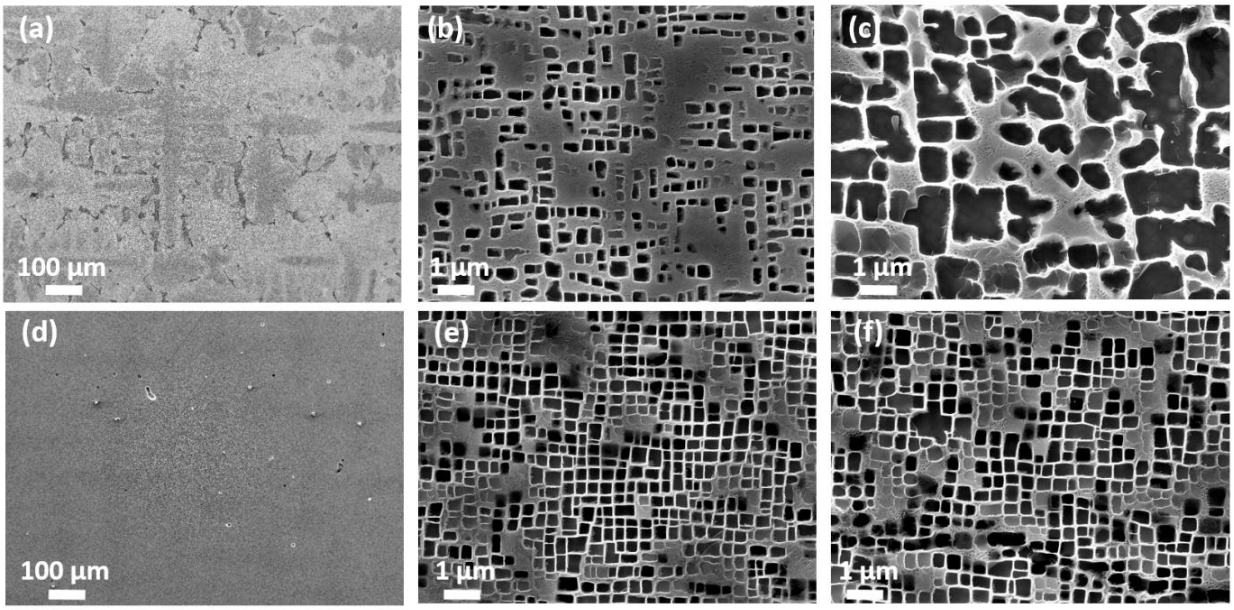

Fig. 93 – Cast dendritic structure (a, d) and γ/γ′ microstructure in primary dendrite arms (b, e) and in interdendritic spacings (c, f) of an experimental 3rd generation 5.4 wt. pct Re-containing SX alloy. An optimized ST+ agings schedule has been applied for (d, e, f) while only agings (no ST) were applied for (a, b, c) microstructures. (authors own works)

3.1.2) Aging heat treatments

Differently from other precipitate strengthened materials like aluminum alloys, maraging steels or Inconel 718, aging heat treatments applied to γ/γ' SX alloys do not trigger the γ' precipitation. Indeed, almost all the γ' precipitates have already formed during cooling from the ST temperatures, even for fast cooling rates of up to 500°C/min [71]. Industrially, typical cooling rates from the solution treatment temperatures are in the 200 – 400 C/min for aero-engines components [72-74], and slower for large blades and vanes used in industrial gas turbines due to their thermal mass [73, 75]. Hence, from a bulk microstructure point of view, aging heat treatments have the main purpose to adjust the size and morphology of γ' precipitates, so as to achieve a regular array of cubical precipitates having an average edge length of nearly 400-500 nm. In fact, it is well admitted in the literature that such a microstructure is the most desirable to maximize creep, tensile and fatigue properties ~ [001] oriented components in a very wide temperature range (i.e. from 700°C up to 1,000-1,100°C), whatever the alloy composition [2, 62-64, 74, 76], by favoring an homogeneous plastic activity in the γ matrix [77].

A typical example of the to γ/γ' microstructure evolution in primary dendrite arms of the AM3 1st generation Ni-based SX alloy is given in Fig. 14 (see composition in Table 1). Starting from a coarse and erratic precipitation state after Bridgman casting (due to slow cooling rate), a fine precipitation of nearly 100-200 nm in size is obtained after the ST followed by a 300°C/min cooling rate. During the first aging at 1080°C for 6h, followed by air quench (AQ), a very regular array of cubical precipitates is obtained, as observed in Fig. 104. Even if it is recalled that the duration and temperature of the first aging heat treatment are mainly defined to ensure a good interdiffusion between the substrate and the bond coat of either β-(Pt)NiAl or MCrAlY (M = Ni, Co, Ta) type (see chapter 12 of this book) and a sufficient pre-oxidation of the bond coat before ceramic top coat deposition, in addition to cost considerations, most of first aging heat treatment temperatures are within the 1,050°C-1,170°C temperature range [78], ensuring this regular microstructure. In fact, in such a temperature range, the natural lattice mismatch (i.e. without any application of external stress) is close to being maximum in absolute value [79-87], ensuring a very huge level of long range internal stresses [88, 89], hence favoring this very regular cuboidal γ/γ' microstructure. Finally, the last aging heat treatment performed at lower temperatures (typically between 750°C and 900°C) has the main purpose to relax residual stresses introduced during all processing steps (e.g. broaching of the blade root, laser cooling holes perforation, minor profile grinding to correct geometrical defects …). From a microstructure point of view, this last aging leads to thinner γ matrix channels (see Fig. 14) thanks to the higher γ' content at temperatures below 900°C (the γ' content is of nearly 70% in most of Ni-

based SX alloys from room temperature up to ~ 800-900°C, and then slowly decrease up to the γ' solvus temperature [90-96]) compared to the temperature employed during first aging heat treatment. This decrease of the γ channel width is known to limit dislocation mobility [77, 97] and, consequently, to improve creep and tensile properties [74, 94, 98-100].

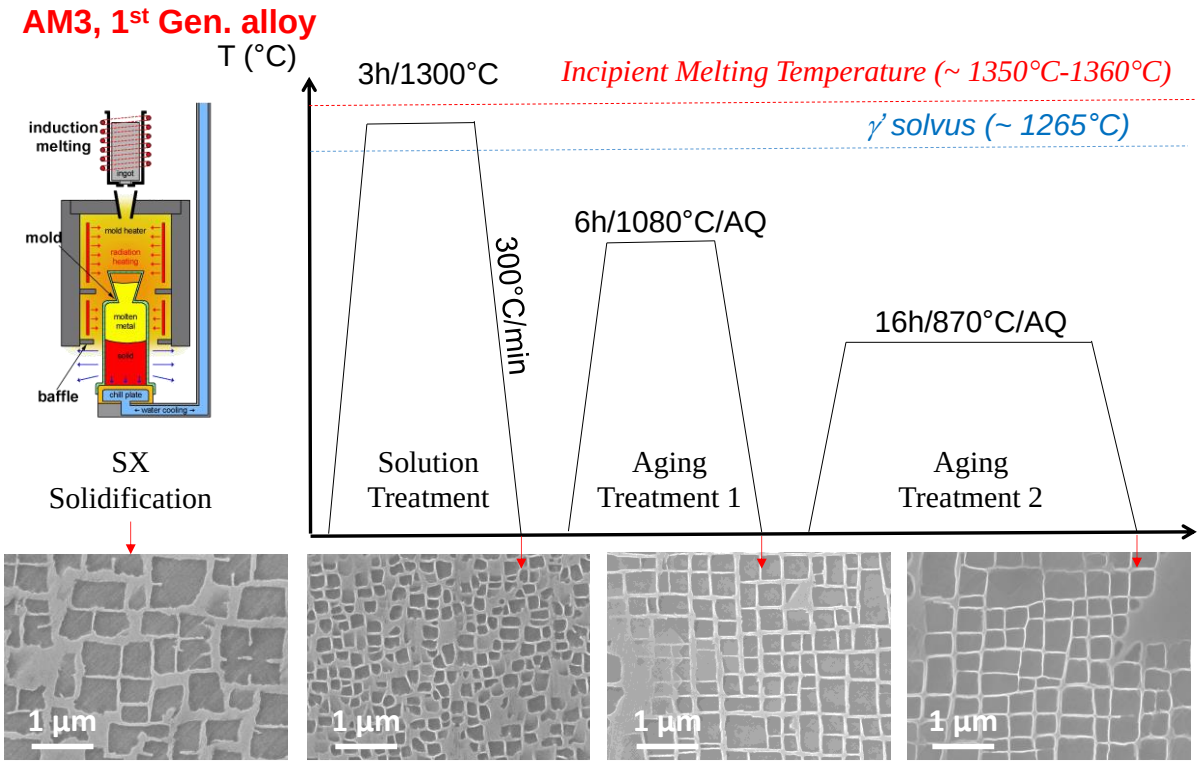

Fig. 104 – γ/γ' microstructure evolution in primary dendrite arms of AM3 1st generation Ni-based SX superalloy from as cast to fully heat treated state. (authors own works)

3.2) Defects and optimizations

3.2.1) Incipient melting

The occurrence of incipient melting (see example in Fig. 10a) during solution treatment becomes an issue for Ni-based SX alloys with a high amount of refractory elements such a Re, W, Ta and Mo. Indeed, by increasing the content of such elements, the degree of chemical segregation is increased, overall leading to a lower temperature for incipient melting within interdendritic spacings while the γ' solvus temperature is increased. Overall, the heat treatment "window" becomes (very) narrow if one wants to dissolve as much as possible γ/γ' eutectics pools without reaching incipient melting [58, 59, 101]. This is typically the case for alloys such as CMSX-10 alloys family (see CMSX-10K composition in Table 1) for which

intricate ST schedules have to be designed [58, 59, 102-104]. Despite very few studies have been performed on the consequences of incipient melting on subsequent mechanical properties, it is interesting to notice that one group in China is proposing a new type of ST approach, including incipient melting and re-solutionning afterwards at a close-to-solvus temperature so as to rejuvenate all melted areas [105]. Improved creep strength have been obtained for a 3rd generation alloy with such a modified ST, since the chemical homogeneity is better across the dendritic structure compared to "standard" step-wise ST ending just below the incipient melting temperature [105]. Very recently, it has even been shown by L.M. Bortoluci Ormastroni that incipient melting can be tolerated in CMSX-4 Plus 3rd generation SX alloy after ST provided that localized melting is not accompanied by a detrimental pore growth [56]. In fact, local melted areas re-solidify in epitaxial relationship with the un-melted metal during final ST cooling and subsequent aging heat treatments restore an acceptable γ/γ' microstructure within and in the vicinity melted area. It was shown that an area fraction of up to 10 pct. of incipient melting has no detrimental impact on tensile, creep and fatigue properties [56].

3.2.2) Optimizations

Due to the cost added to the overall price of SX components by heat treatments, especially the solution heat treatment, reducing the duration and/or temperature of ST to the strictly necessary in terms of microstructure/mechanical properties quality is highly desirable. Usually, in such complex multi-element alloys, one of the simplest way to estimate the time necessary for ST is to assume that the completeness of this heat treatment is controlled by the diffusion of the slowest diffusion element [69, 106, 107], which is often rhenium for 2nd, 3rd and 4th generation alloys, while it is tungsten for most of 1st generation alloys. A ST is considered as completed once such an element has been able to diffuse over a characteristic length L which generally corresponds to the distance between the primary dendrite arm and interdendritic spacing centers. This distance can be calculated according to Eq. 3, knowing the apparent diffusion coefficient D of the least diffusive element [69, 108, 109], which is temperature dependent:

$$L = \sqrt{D * t} \tag{3}$$

From this equation, it is then possible to obtain an estimation of the required ST duration t to achieve acceptable chemical homogeneity. It is clearly seen that the smaller will be the L value, the shorter/cooler can be the solution heat treatments. This is clearly the case

for AM1 SX alloy, in which almost no more remaining eutectics has been observed after an accelerated (LMC) solidification compared to a standard one, using the same solution treatment (see Fig. 17 later on in this section) [22]. More recently, it has been observed even more impressive possibilities in ST time/temperature reduction considering quasi-SX solidification achieved by Selective Electron Beam Melting [3, 110, 111].

Over the last 10 years, different numerical tools have been developed to achieve much more reliable previsions of the chemical homogenization during ST, based on multi-component diffusion databases and taking into account the initial dendritic chemical heterogeneity in a phase field approach [112]. The limitations of these approaches are that they are much more time consuming and they require the knowledge of the initial distribution of elements in the as-cast state. The same applies regarding the optimization of the precipitate size during aging heat treatments using phase-field approaches [113-117] at the expanse of very simple and efficient mean-field Lifshitz-Slyozov-Wagner (LSW) models [118, 119].

4) Mechanical properties sensitivity to the processing parameters

4.1) Creep and tensile properties

As already mentioned earlier in this chapter, solution and aging heat treatments have mainly been designed so as to achieve the best degree of chemical homogeneity across the dendritic and a regular array of cuboidal γ' precipitates with an average edge length of nearly 400-500 nm. No exception to this "rule of thumbs" can be noticed in the open literature for ~ <001> oriented components (the usual crystallographic orientation along the profile of blades) while it is known that the optimal precipitate edge length in terms of creep resistance for ~ <111> oriented SX specimens is around 200 nm [64]. This optimal precipitate size and regularity is also one of the targets to be reached for serviced components using rejuvenation procedures involving a ST and/or HIPping procedure after several hours of use [114, 120-122].

However, processing of components involves many different steps in addition to the "state-of-the-art" solution and aging heat treatments and industrial practices may lead, sometimes, to variation in cooling rates at the end of, e.g., the solution treatment. If the effect of the ST cooling rate has been widely studied for polycristalline disk alloys [123-125], very few papers have attempted to investigate this parameter on creep properties of Ni-based DS/SX alloys [72, 74]. Figure 115 presents the consequences of this parameter on creep properties of AM3 alloy. The solution cooling rate was varied from 10°C/min up to 300°C/min, covering possible cooling rates encountered for high pressure turbine blades used

in industrial gas turbines, large civil aero-engines and turboshaft engines for helicopters. The slower the cooling rate, the coarser the γ' precipitation and the more irregular the morphology of precipitates. At the fastest cooling rate, the optimum cuboidal microstructure is obtained as observed in Fig. 115. For an intermediate cooling rate of 80°C/min, the precipitation is irregular across the dendritic structure, with cuboids within primary dendrite arms (due to a locally higher γ/γ' misfit resulting from the remaining chemical microsegregation) and a coarser precipitation within interdendritic spacings. For the slowest cooling rate, very coarse and interconnected precipitates are obtained, with a second population of very fine secondary γ' precipitates. In this study, it was shown that the slower the cooling rate, the lower the yield stress in tension from room temperature up to 950°C, and the lower the isothermal and non-isothermal creep properties [74]. As observed in Fig. 126, having a ST cooling rate of 10°C/min corresponds to a spectacular decrease in creep strength of nearly 50°C in all the investigated temperature range (i.e. from 750°C up to 1050°C) compared to a ST cooling rate of 300°C/min. The creep properties with a ST cooling rate of 80°C/min lie in between these two extremes, closer to 300°C/min cooling rate [74]. It is then of the utmost importance to have the fastest possible cooling rate after the solution heat treatment to achieve a fine distribution of precipitates that can be adjusted in morphology and size afterwards by aging heat treatments. This is the reason why most of solution heat treatment furnaces are equipped with forced convection devices (e.g. gas fan cooling systems) to achieve the desired cooling rates, especially for large industrial gas turbines components. Coupled fluid-thermic modeling of the cooling gas flow in such furnaces is highly desired to optimize location of components and their cooling histories [126, 127].

To summarize, creep properties of Ni-based SX superalloys are mainly dependent on the regularity of the γ/γ' microstructure across the dendritic structure and the ability to reach a cubical γ' whose average edge length is in the 400-500 nm range, i.e. on the solution heat treatment (mainly) and agings. It is however weakly dependent on the size of the casting pore size, as observed by Steuer et al. [22]. A large casting pore size and heterogeneous distribution of pores as observed in Fig. 9a may only affect creep ductility and lifetime, but with a limited effect on both primary and secondary creep stages. A typical maximum acceptable porosity level for SX components from a creep point of view is in the 0.5-1% range.

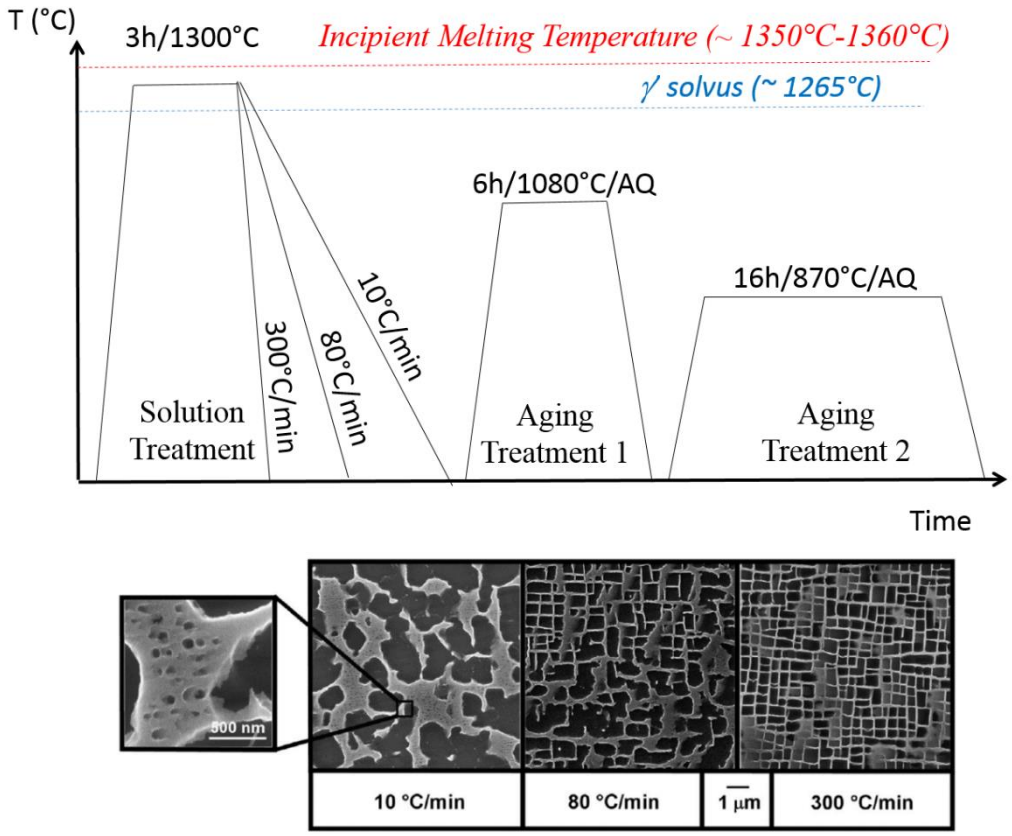

Cooling rate			10 °C/min	80 °C/min	300 °C/min
Cube length/diameter	Overall	nm	1575 ± 1231	471 ± 245	447 ± 185
	Dendritic	nm	1646 ± 1296	444 ± 206	423 ± 157
	Interdendritic	nm	1511 ± 1168	506 ± 283	485 ± 217
Channel width	Overall	nm	249 ± 109	105 ± 53	85 ± 63

Fig. 115 – Evolution of γ/γ' microstructure as a function of the ST cooling rate for AM3 1st generation SX alloy. Adapted from [74].

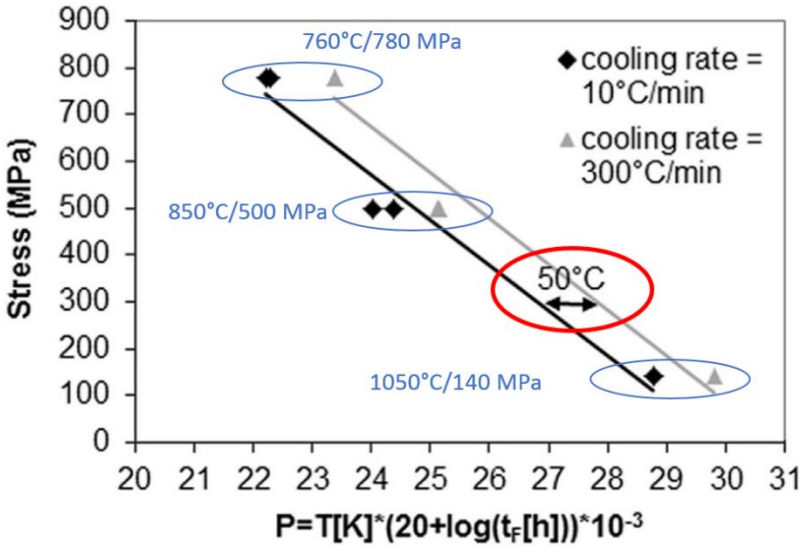

Fig. 126 – Creep properties dependence (Larson-Miller diagram) of AM3 1st generation SX superalloy as a function of the ST cooling rate. Adapted from [74].

4.2) Fatigue properties

Fatigue properties, in the absence of any contribution of oxidation, are mostly dependent to the solidification defects, and more particularly to the casting pore size [22, 128, 129]. One of the pioneering study has been conducted by Lamm and Singer using PWA 1483 1st generation SX alloy used for land-based gas turbines for power generation, showing that the finer the dendritic structure (especially primary dendrite arm spacings), the higher the high cycle fatigue (HCF) at 800°C/R_σ = -1/f = 95 Hz [21]. Such an issue was deepen later on by C. Brundidge, using René N5 2nd generation SX alloy, and a modified Ta-rich version of this alloy and both "standard" Bridgman solidification and Liquid Metal Cooling (LMC) [11, 130, 131]. As expected, increasing the solidification rate led to a finer dendritic structure (see Fig. 137) and to smaller casting pores, especially the largest ones, the volume fraction of pores being almost the same. As a consequence of this decrease in the largest pore size, an improvement in low cycle fatigue (LCF) properties was obtained while creep properties were hardly affected by the change in solidification process.

A better understanding was then obtained by S. Steuer et al. [22] and more recently, by A. Cervellon et al. [98, 132]. Indeed, as observed Fig. 148, the smaller the pore size is, the higher is the LCF life of AM1 1st generation SX alloy (see composition in Table 1) at 750°C//R_σ = -1/f = 0.5 Hz. An improvement of up to a factor 4 can be achieved in this condition using the LMC solidification process. At higher temperatures (e.g. 950°C and more), when oxidation is more active, this benefit is not observed anymore since crack initiation occurs at the surface. It was however shown that the casting pore size (and hence the solidification process) intrinsically controls the fatigue life at such a high temperature if tests are performed in high vacuum [22] or at high frequencies [55, 98, 132], such as the ones encountered by airfoils during transient engine regimes corresponding to the excitation of one of their fundamental resonance mode. Indeed, Fig.159 shows that the very high cycle fatigue (VHCF) life of AM1 1st generation SX alloy can be improved by a factor of 5 using an LMC solidification process compared to a Bridgman one. Applying a HIPping process is even more efficient according to this figure, by (almost) closing all casting pores. As a fundamental understanding, this improvement in fatigue properties by reducing the casting pore size results from a longer time spent in the very short crack propagation (the so-called micro-propagation domain) which can be into account using newly developed fatigue life criteria [22, 55, 56, 98, 132].

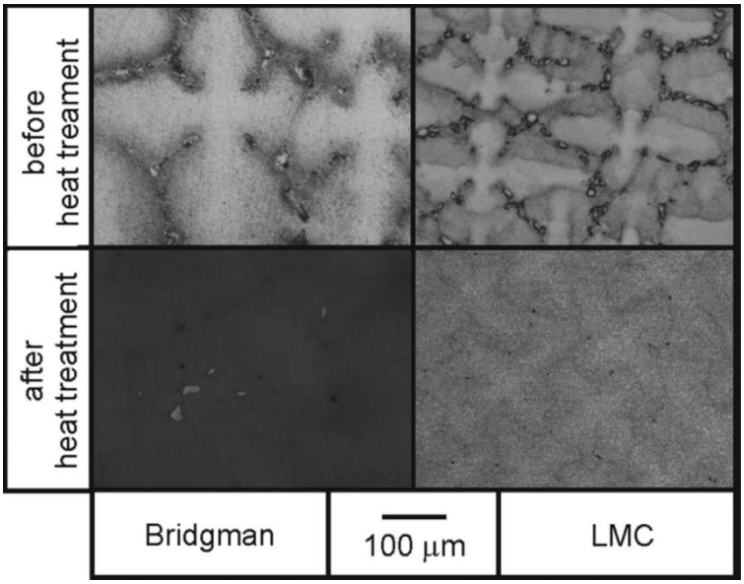

Fig. 137 – Dendritic structure of AM1 1st generation SX alloy after Bridgman and LMC processing. Adapted from [22].

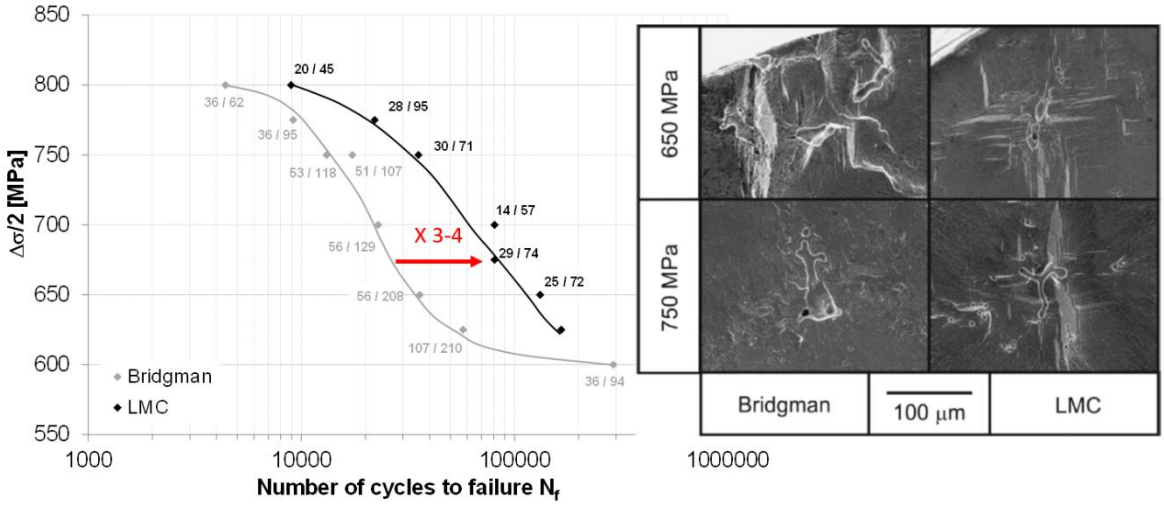

Fig. 148 – LCF properties of AM1 1st generation SX alloy at 750°C/R_σ = 0.05/f = 0.5 Hz as a function of the solidification process (a) and crack initiation sites (b). Numbers in (a) for each datapoint correspond to the size of the pore serving as a crack initiation site expressed as either the diameter of the smallest circle in which the pore can be included or the projected are of this pore. Adapted from [22].

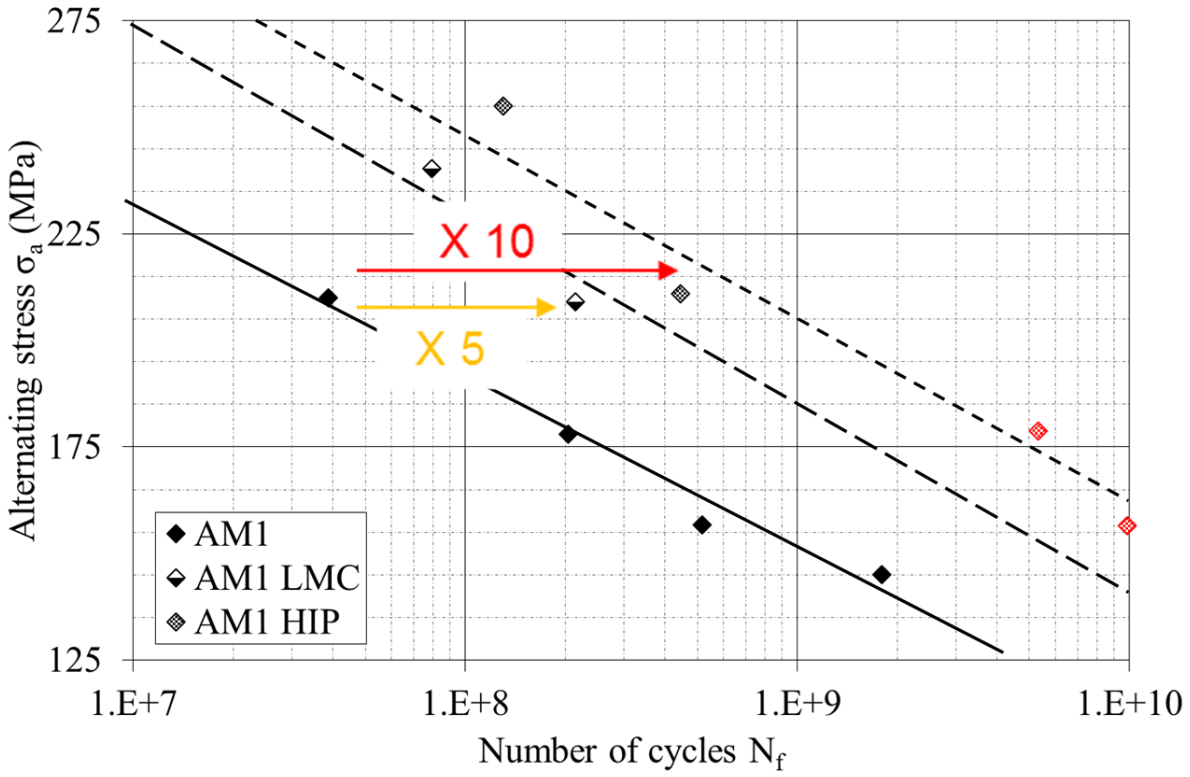

Fig. 159 – Effect of the pore size on VHCF properties of AM1 1st generation SX alloy at 1,000°C/Rε = -1/f = 20,000 Hz. Adapted from [132, 133].

In summary, fatigue properties are mainly dependent on the solidification process when environment has a limited contribution to the crack initiation processes. Accelerating the solidification process is then a very reliable way to increase service life of Ni-based SX components, especially for internally cooled ones known to be very sensitive to fatigue cracking during their service life [134].

5) Conclusions

Presentation has been given of the general features dealing with casting and heat treatments used for the production of SX components, including historical background and current trends, mainly dealing with modeling and simulation.

Based upon historical perspectives, two main improvements can be highlighted considering the use of nickel base superalloys: *i*- alloys with always better creep properties at increased operating temperature and *ii*- complicated air cooling as part of the component design. These were the results of collaborations between metallurgists and mechanical engineers, while processing had to adapt and find solutions to deliver the products. The yield rate is still low for single crystal casting, typically reaching 70% as a consequence of the

demand for very high quality. And because of the evolution of the alloy compositions, further steps are required for the products, such as the deposit of a thermal barriers coating. Yet this was not part of the criteria for the design of the last generation superalloys and many such alloys could not be introduced in engines because of the absence of thermal barriers coatings. So despite the fact that metallurgist could demonstrate always better intrinsic mechanical properties of new alloys composition, other factors prevented their use.

Processing capabilities and the entire processing route were not or very little considered so engineers and processing teams had to adapt forming processes of the alloys from its original formulation. As a consequence alloys were proposed with enhanced creep properties at high temperature. However, no coating could be designed for these alloys which are not in-use for SX blades. This shows that a SX component is a very sophisticated item that, more than in the past, needs collaborative efforts to bring innovative ideas into a working product. Enhanced synergetic strategies are required that would bring engine efficiency always higher as a result of a team work gathering teams of process engineers, metallurgists and physicists to create enhanced materials science products.

Acknowledgements

The authors would like to thank Dr. Boyd Mueller of Arconic Inc. (formerly of Howmet Corporation), Dilip K. Banerjee of the National Institute of Standards and Technology (NIST) and Dr. Virginie Jaquet of SAFRAN Tech for providing some of the illustrations. Dr. Jérémy Rame (SAFRAN Aircraft Engines), Dr. Zéline Hervier (SAFRAN Helicopter Engines) and Dr. Lorena Mataveli Suave (SAFRAN Tech) are also acknowledged for fruitful discussions and technical exchanges on heat treatments and mechanical characterizations of Ni-based SX superalloys. JC is grateful to Pr. Tresa M. Pollock (University of California – Santa Barbara/Materials Department) for sharing joint experiments on LMC processed Ni-based SX superalloys and to Dr. Alice Cervellon (formerly at ISAE-ENSMA/Institut Pprime and now at the University of California – Santa Barbara/Materials Department) for her “VHCF” contributions. Luciana Bortoluci Ormastroni (M.Sc. from ISAE-ENSMA, currently PhD student at ISAE-ENSMA Institut Pprime) is acknowledged for her contributions on solution heat treatments.

References

1. M. Durand-Charre, *The microstructure of superalloys*. 1997: Gordon and Breach Science Publishers.
2. R.C. Reed, *The Superalloys - Fundamentals and Applications*. 2006, Cambridge, UK: Cambridge University Press.

3. C. Körner, M. Ramsperger, C. Meid, D. Bürger, P. Wollgramm, M. Bartsch, and G. Eggeler, *Microstructure and mechanical properties of CMSX-4 single crystals prepared by additive manufacturing.* Metallurgical and Materials Transactions A, 2018. **49**(9): p. 3781-3792.
4. P. Caron. *High γ′ solvus new generation nickel-based superalloys for single crystal turbine blade applications*. in *Superalloys 2000*. 2000. Seven Springs, PA, USA: TMS. p. 737-746.
5. R. Reed, T. Tao, and N. Warnken, *Alloys-by-design: application to nickel-based single crystal superalloys.* Acta Materialia, 2009. **57**(19): p. 5898-5913.
6. *Casting*. ASM Handbook Vol. 15. 2008, Metals Park, OH, USA: ASM International.
7. C.-A. Gandin, M. Rappaz, and R. Tintillier, *Three-dimensional probabilistic simulation of solidification grain structures: Application to superalloy precision castings.* Metallurgical Transactions A, 1993. **24**(2): p. 467-479.
8. C.-A. Gandin, M. Rappaz, and R. Tintillier, *3-dimensional simulation of the grain formation in investment castings.* Metallurgical and Materials Transactions A, 1994. **25**(3): p. 629-635.
9. F.L. VerSnyder and M.E. Shank, *The development of columnar grain and single crystal high temperature materials through directional solidification.* Materials Science and Engineering, 1970. **6**: p. 213-247.
10. A. Elliott, T. Pollock, S. Tin, W. King, S.-C. Huang, and M. Gigliotti, *Directional solidification of large superalloy castings with radiation and liquid-metal cooling: A comparative assessment.* Metallurgical and Materials Transactions A, 2004. **35**(10): p. 3221-3231.
11. C.L. Brundidge, D.v. Drasek, B. Wang, and T.M. Pollock, *Structure Refinement by a Liquid Metal Cooling Solidification Process for Single-Crystal Nickel-Base Superalloys.* Metallurgical and Materials Transactions A, 2012. **43**: p. 965-976.
12. W. Kurz and D.J. Fisher, *Fundamentals of Solidification*. 1989, Aedermannsdorf, Switzerland Trans Tech Publications Ltd.
13. G. Bouse and J. Mihalisin, *Metallurgy of investment cast superalloy components*, in *Superalloys, supercomposites and superceramics*, J.K. Tien and T. Caulfield, Editors. 1989, Academic Press. p. 99-148.
14. B. Walser, F. Staub, R. Wege, and J. Wortmann, *An alternative single crystal manufacturing process for gas turbine blades.* MTU. focus, 1989. **1**: p. 21-28.
15. A. Kounitzky, J. Wortmann, and P. Agarwal, *A single crystal casting process for high-temperature components.* Materials & Design, 1991. **12**(6): p. 323-330.
16. C.-A. Gandin, *From constrained to unconstrained growth during directional solidification.* Acta Materialia, 2000. **48**(10): p. 2483-2501.
17. J.A. Dantzig and M. Rappaz, *Solidification: -Revised & Expanded*. 2016: EPFL press.
18. A. Giamei and J. Tschinkel, *Liquid metal cooling: a new solidification technique.* Metallurgical transactions A, 1976. **7**(9): p. 1427-1434.
19. L.D. Graham and B.L. Rauguth, *Method and device for casting a metal article using a fluidized bed*. 2000: European patent EP 1153681 A1 20011114.
20. M. Hofmeister, M. Franke, C. Koerner, and R. Singer, *Single crystal casting with fluidized carbon bed cooling: a process innovation for quality improvement and cost reduction.* Metallurgical and Materials Transactions B, 2017. **48**(6): p. 3132-3142.
21. M. Lamm and R.F. Singer, *The Effect of Casting Conditions on the High-Cycle Fatigue Properties of the Single-Crystal Nickel-Base Superalloy PWA 1483.* Metallurgical and Materials Transactions A, 2007. **38A**: p. 1177-1183.

22. S. Steuer, P. Villechaise, T.M. Pollock, and J. Cormier, *Benefits of high gradient solidification for creep and low cycle fatigue of AM1 single crystal superalloy.* Material Science and Engineering A, 2015. **645**: p. 109-115.
23. W. Xuan, J. Lan, H. Liu, C. Li, J. Wang, W. Ren, Y. Zhong, X. Li, and Z. Ren, *Effects of a High Magnetic Field on the Microstructure of Ni-Based Single-Crystal Superalloys During Directional Solidification.* Metallurgical and Materials Transactions A, 2017. **48**: p. 3804-3813.
24. C.A. Gandin, M. Rappaz, D. West, and B. Adams, *Grain texture evolution during the columnar growth of dendritic alloys.* Metallurgical and Materials Transactions A, 1995. **26**(6): p. 1543-1551.
25. A. Pineau, G. Guillemot, D. Tourret, A. Karma, and C.-A. Gandin, *Growth competition between columnar dendritic grains–Cellular automaton versus phase field modeling.* Acta Materialia, 2018. **155**: p. 286-301.
26. T. Takaki, S. Sakane, M. Ohno, Y. Shibuta, T. Aoki, and C.-A. Gandin, *Competitive grain growth during directional solidification of a polycrystalline binary alloy: three-dimensional large-scale phase-field study.* Materialia, 2018. **1**: p. 104-113.
27. B.A. Mueller and R.A. Spicer. *Land-based turbine casting initiative*. in *Advanced Turbine Systems Annual Program Review Meeting*. 1995. Oak Ridge National Lab., TN, USA. p. 161-170.
28. P. Carter, D. Cox, C.-A. Gandin, and R.C. Reed, *Process modelling of grain selection during the solidification of single crystal superalloy castings.* Materials Science and Engineering: A, 2000. **280**(2): p. 233-246.
29. C.-A. Gandin, J.-L. Desbiolles, M. Rappaz, and P. Thevoz, *A three-dimensional cellular automation-finite element model for the prediction of solidification grain structures.* Metallurgical and Materials Transactions A, 1999. **30**(12): p. 3153-3165.
30. M. Rezaei, A. Kermanpur, and F. Sadeghi, *Effects of withdrawal rate and starter block size on crystal orientation of a single crystal Ni-based superalloy.* Journal of Crystal Growth, 2018. **485**: p. 19-27.
31. Q. Xu, C. Yang, H. Zhang, X. Yan, N. Tang, and B. Liu, *Multiscale modeling and simulation of directional solidification process of Ni-based superalloy turbine blade casting.* Metals, 2018. **8**: p. 632.
32. C.-A. Gandin, R. Schaefer, and M. Rappaz, *Analytical and numerical predictions of dendritic grain envelopes.* Acta Materialia, 1996. **44**(8): p. 3339-3347.
33. A. de Bussac and C.-A. Gandin, *Prediction of a process window for the investment casting of dendritic single crystals.* Materials Science and Engineering: A, 1997. **237**(1): p. 35-42.
34. U. Paul, P. Sahm, and D. Goldschmidt, *Inhomogeneities in single-crystal components.* Materials Science and Engineering: A, 1993. **173**(1-2): p. 49-54.
35. R. Schaefer, M. Vaudin, B. Mueller, C. Choi, and J. Szekely. *Generation of defects in single crystal components by dendrite remelting*. in *7th conference Modeling of Casting, Welding and Advanced Solidification Processes* 1995: TMS, Warrendale, PA (United States). p. 593-600.
36. H. Ben Hamouda, *Modélisation et Simulation de la structure de solidification dans les superalliages base-nickel : Application AM1*, PhD Thesis, in *CEMEF*. 2012, MINES ParisTech: Sophia Antipolis.
37. N. Warnken, D. Ma, A. Drevermann, R.C. Reed, S.G. Fries, and I. Steinbach, *Phase-field modelling of as-cast microstructure evolution in nickel-based superalloys.* Acta Materialia, 2009. **57**: p. 5862-5875.
38. G. Reinhart, D. Grange, L. Abou-Khalil, N. Mangelinck-Noël, N.T. Niane, V. Maguin, G. Guillemot, C.-A. Gandin, and H. Nguyen-Thi, *Impact of solute flow*

during directional solidification of a Ni-based alloy: in situ and real-time X-radiography. Acta Materialia, 2020. **In press**.
39. S. Copley, A.F. Giamei, S. Johnson, and M. Hornbecker, *The origin of freckles in unidirectionally solidified castings.* Metallurgical Transactions, 1970. **1**(8): p. 2193-2204.
40. S. Tin and T. Pollock, *Predicting freckle formation in single crystal Ni-base superalloys.* Journal of Materials Science, 2004. **39**(24): p. 7199-7205.
41. C. Beckermann, J. Gu, and W.J. Boettinger, *Development of a freckle predictor via Rayleigh number method for single-crystal nickel-base superalloy castings.* Metallurgical and Materials Transactions A, 2000. **31**(10): p. 2545-2557.
42. J. Ramirez and C. Beckermann, *Evaluation of a Rayleigh-number-based freckle criterion for Pb-Sn alloys and Ni-base superalloys.* Metallurgical and Materials Transactions A, 2003. **34**(7): p. 1525-1536.
43. A. Saad, C.-A. Gandin, M. Bellet, N. Shevchenko, and S. Eckert, *Simulation of Channel Segregation During Directional Solidification of In—75 wt pct Ga. Qualitative Comparison with InSitu Observations.* Metallurgical and Materials Transactions A, 2015. **46**(11): p. 4886-4897.
44. D.K. Banerjee and K.O. Yu, *Investment casting*, in *Modeling for Casting and Solidification Processing*, K.O. Yu, Editor. 2002, CRC Press. p. 333-372.
45. D. Sun, L. Liu, T. Huang, W. Yang, C. He, Z. Li, J. Zhang, and H. Fu, *Formation of Lateral Sliver Defects in the Platform Region of Single-Crystal Superalloy Turbine Blades.* Metallurgical and Materials Transactions A, 2019. **50**(3): p. 1119-1124.
46. J. Aveson, G. Reinhart, C. Goddard, H. Nguyen-Thi, N. Mangelinck-Noël, A. Tandjaoui, J. Davenport, N. Warnken, F. Di Gioacchino, and T. Lafford, *On the Deformation of Dendrites During Directional Solidification of a Nickel-Based Superalloy.* Metallurgical and Materials Transactions A, 2019. **50**(11): p. 5234-5241.
47. N. Siredey, M.B. Boufoussi, S. Denis, and J. Lacaze, *Dendritic growth and crystalline quality of nickel-base single grains.* Journal of Crystal Growth, 1993. **130**(1-2): p. 132-146.
48. D. Cox, B. Roebuck, C. Rae, and R. Reed, *Recrystallisation of single crystal superalloy CMSX–4.* Materials Science and Technology, 2003. **19**(4): p. 440-446.
49. Z. Li, X. Fan, Q. Xu, and B. Liu, *Influence of deformation temperature on recrystallization in a Ni-based single crystal superalloy.* Materials Letters, 2015. **160**: p. 318-322.
50. C. Panwisawas, H. Mathur, J. Gebelin, D. Putman, P. Withey, N. Warnken, C. Rae, and R. Reed. *Prediction of plastic strain for recrystallisation during investment casting of single crystal superalloys*. in *Superalloys 2012*. 2012. Seven Springs, PA, USA: TMS. p. 547-556.
51. A. Epishin, B. Fedelich, T. Link, T. Feldmann, and I.L. Svetlov, *Pore annihilation in a single-crystal nickelbase superalloy during hot isostatic pressing: experiment and modelling.* Material Science and Engineering, 2013. **586**: p. 342-349.
52. A. Epishin, T. Link, H. Klingelhoffer, P. Portella, and B. Fedelich, *Creep damage of single-crystal superalloys: mechanisms and effect on low cyle fatigue.* Materials At High Temperarture, 2010. **23**(1): p. 53-59.
53. J.-B. le Graverend, J. Adrien, and J. Cormier, *Ex-situ X-ray Tomography Characterization of Porosity During High-Temperature Creep in a Ni-based Single-Crystal Superalloy: Toward Understanding What Damage Is.* Material Science & Engineering A, 2017. **695**: p. 367-378.

54. T. Link, S. Zabler, A. Epishin, A. Haibel, M. Bansal, and X. Thibault, *Synchrotron tomography of porosity in single-crystal nickel-base superalloys.* Materials Science and Engineering, 2006. **A 425**: p. 47-54.

55. A. Cervellon, S. Hémery, P. Kürnsteiner, B. Gault, P. Kontis, and J. Cormier, *Crack initiation mechanisms during very high cycle fatigue of Ni-based single crystal superalloys at high temperature.* Acta Materialia, 2020. **188**: p. 131-144.
56. L.M. Bortoluci Ormastroni, L. Mataveli Suave, A. Cervellon, P. Villechaise, and J. Cormier, *LCF, HCF and VHCF life sensitivity to solution heat treatment of a third-generation Ni-based single crystal superalloy.* International Journal of Fatigue, 2020. **130**: p. 105247.
57. A. Heckl, R. Rettig, and R. Singer, *Solidification characteristics and segregation behavior of nickel-base superalloys in dependence on different rhenium and ruthenium contents.* Metallurgical and Materials Transactions A, 2010. **41**(1): p. 202.
58. H.T. Pang, N. D'Souza, H. Dong, H.J. Stone, and C.M. Rae, *Detailed Analysis of the Solution Heat Treatment of a Third-Generation Single-Crystal Nickel-Based Superalloy CMSX-10K®.* Metallurgical and Materials Transactions A, 2016. **47**(2): p. 889-906.
59. H.T. Pang, L. Zhang, R.A. Hobbs, H.J. Stone, and C.M. Rae, *Solution heat treatment optimization of fourth-generation single-crystal nickel-base superalloys.* Metallurgical and Materials Transactions A, 2012. **43**(9): p. 3264-3282.
60. Y. Zhang, L. Liu, T. Huang, Q. Yue, D. Sun, J. Zhang, W. Yang, H. Su, and H. Fu, *Investigation on a ramp solution heat treatment for a third generation nickel-based single crystal superalloy.* Journal of Alloys and Compounds, 2017. **723**: p. 922-929.
61. S. Hegde, R. Kearsey, and J. Beddoes. *Design of solutionizing heat treatments for an experimental single crystal superalloy*. in *Superalloys 2008*. 2008. Seven Springs, PA, USA: TMS. p. 301-310.
62. P. Caron, P.J. Henderson, T. Khan, and M. McLean, *On the effects of heat treatments on the creep behaviour of a single crystal superalloy.* Scripta Metallurgica, 1986. **20**(6): p. 875-880.
63. P. Caron and T. Khan, *Improvement of creep strenght in a nickel-base single crystal superalloy by heat treatment.* Materials Science and Engineering, 1983. **61**: p. 173-194.
64. P. Caron, Y. Ohta, Y.G. Nakagawa, and T. Khan. *Creep deformation anisotropy in single crystal superalloys*. in *Superalloys 1988*. 1988. Seven Springs, PA, USA: TMS. p. 215-224.
65. J.J. Jackson, M.J. Donachie, R.J. Henricks, and M. Gell, *The effects of volume percent of fine γ′ on creep in DS Mar-M200 + Hf.* Metallurgical Transactions, 1977. **8A**(October): p. 1615-1620.
66. W. Walston, J. Schaeffer, and W. Murphy, *A new type of microstructural instability in superalloys-SRZ.* in *Superalloys 1996*. 1996. Seven Springs, PA, USA: TMS. p. 9-18.
67. L. Huang, X. Sun, H. Guan, and Z. Hu, *Oxidation behavior of the single-crystal Ni-base superalloy DD32 in air at 900, 1000, and 1100° C.* Oxidation of metals, 2006. **65**(5-6): p. 391-408.
68. M. Li, X. Sun, J. Li, Z. Zhang, T. Jin, H. Guan, and Z. Hu, *Oxidation behavior of a single-crystal Ni-base superalloy in air. I: at 800 and 900 C.* Oxidation of Metals, 2003. **59**(5-6): p. 591-605.
69. B.S. Bokstein, A.I. Epishin, T. Link, V.A. Esin, A.O. Rodin, and I.L. Svetlov, *Model for the porosity growth in single-crystal nickel-base superalloys during homogenization.* Scripta Materiala, 2007. **57**: p. 801-804.

70. A.I. Epishin, T. Link, B. Fedelich, I.L. Svetlov, and E.R. Golubovskiy, *Hot isostatic pressing of single-crystal nickel-base superalloys: Mechanism of pore closure and effect on Mechanical properties.* MATEC Web of Conferences, 2014. **14** (EUROSUPERALLOYS 2014 – 2nd European Symposium on Superalloys and their Applications): p. 08003.
71. T. Grosdidier, A. Hazotte, and A. Simon, *Precipitation and dissolution processes in γ/γ′ single crystal nickel-based superalloys.* Material Science and Engineering A, 1998. **256**: p. 183-196.
72. M.-S. Chiou, S.-R. Jian, A.-C. Yeh, C.-M. Kuo, and J.-Y. Juang, *High temperature creep properties of directionally solidified CM-247LC Ni-based superalloy.* Material Science and Engineering A, 2016. **655**: p. 237-243.
73. S. Pierret, *Microstructure of single crystal Ni-based superalloys during blade manufacturing process and creep deformation: a study using X-rays and neutrons*, PhD thesis. 2012, Ecole Polytechnique Fédérale de Lausanne (EPFL): Lausanne (Switzerland).
74. S. Steuer, Z. Hervier, S. Thabart, C. Castaing, T.M. Pollock, and J. Cormier, *Creep behavior under isothermal and non-isothermal conditions of AM3 single crystal superalloy for different solutioning cooling rates.* Material Science and Engineering A, 2014. **601**: p. 145-152.
75. S. Pierret, T. Etter, A. Evans, and H. Van Swygenhoven, *Origin of localized rafting in Ni-based single crystal turbine blades before service and its influence on the mechanical properties.* Acta Materialia, 2013. **61**(5): p. 1478-1488.
76. T.M. Pollock and S. Tin, *Nickel-Based Superalloys for Advanced Turbine Engines: Chemistry, Microstructure, and Properties.* Journal of Propulsion and Power, 2006. **22**(2): p. 361-374.
77. T.M. Pollock and A.S. Argon, *Creep resistance of CMSX-3 nickel base superalloy single crystals.* Acta Metallurgica Materialia, 1992. **40**(1): p. 1-30.
78. M.J. Donachie and S.J. Donachie, *Superalloys: a technical guide*. 2002: ASM international.
79. L.J. Carroll, Q. Feng, and T.M. Pollock, *Interfacial Dislocation Networks and creep in directional coarsened Ru-containing nickel-base single-crystal superalloys.* Metallurgical and Materials Transactions, 2008. **39A**: p. 1290-1307.
80. F. Diologent, P. Caron, T. d'Almeida, A. Jacques, and P. Bastie, *The γ/γ′ mismatch in Ni based superalloys : in situ measurements during a creep test.* Nuclear Instruments and Methods in Physics Reasearch, 2003. **B 200**: p. 346-351.
81. L. Dirand, J. Cormier, A. Jacques, J.-P. Chateau-Cornu, T. Schenk, O. Ferry, and P. Bastie, *Measurement of the effective γ/γ′ lattice mismatch during high temperature creep of Ni-based single crystal superalloy.* Materials Characterization, 2013. **77**: p. 32-46.
82. J.-B. le Graverend, A. Jacques, J. Cormier, O. Ferry, T. Schenk, and J. Mendez, *Creep of a nickel-based single crystal superalloy during very high temperature jumps followed by synchrotron X-Ray diffraction.* Acta Materialia, 2015. **84**: p. 65-79.
83. A. Jacques and P. Bastie, *The evolution of the lattice parameter mismatch of a nickel-based superalloy during a high-temperature creep test.* Philosophical Magazine, 2003. **83**(26): p. 3005-3027.
84. J.X. Zhang, Y. Koizumi, T. Kobayashi, T. Murakumo, and H. Harada, *Strengthening by γ/γ′ Interfacial Dislocation Networks in TMS-162—Toward a Fifth-Generation Single-Crystal Superalloy.* Metallurgical Materials Transactions A, 2004. **35A**: p. 1911-1915.

85. J.X. Zhang, T. Murakumo, Y. Koizumi, and H. Harada, *The influence of interfacial dislocation arrangements in a fourth generation single crystal TMS-138 superalloy on creep properties.* Journal of Materials Science, 2003. **38**: p. 4883-4888.
86. J.X. Zhang, T. Murakumo, Y. Koizumi, T. Kobayashi, H. Harada, and S. Masaki, *Interfacial Dislocation Networks Strengthening a fourth-generation single-crystal TMS-138 superalloy.* Metallurgical and Materials Transactions A, 2002. **33A**(December): p. 3741-3746.
87. J.X. Zhang, J.C. Wang, H. Harada, and Y. Koizumi, *The effect of lattice mismatch on the dislocation motion in superalloys during high-temperature low-stress creep.* Acta Materialia, 2005. **53**: p. 4623-4633.
88. A. Hazotte, *Transformations et contraintes de cohérence dans les superalliages et les intermétalliques de base TiAl.* Matériaux & Techniques, 2009. **97**: p. 23-31.
89. A. Hazotte and A. Simon. *Interactions Contraintes-Microstructure dans l'alliage CMSX2 monocristallin*. in *Colloque National Superalliages Monocristallin*. 1986. Villars de Lans. p. 210-219.
90. P. Caron, C. Ramusat, and F. Diologent. *Influence of the γ′ fraction on the topological inversion during high temperature creep of single crystal superalloys*. in *Superalloys 2008*. 2008. Seven Springs, Champion, PA, USA: TMS, Warrendale, PA. p. 159-167.
91. B. Roebuck, D. Cox, and R.C. Reed, *The temperature dependence of γ′ volume fraction in a Ni-based single crystal superalloy from resistivity measurements.* Scripta Materialia, 2001. **44**: p. 917-921.
92. J. Cormier. *Thermal cycling creep resistance of Ni-based single crystal superalloys* in *Superalloys 2016*. 2016. Seven Springs, Champion, PA, USA: TMS. p. 385-394.
93. R. Giraud, Z. Hervier, J. Cormier, G. Saint-Martin, F. Hamon, X. Milhet, and J. Mendez, *Strain effect on the γ′ dissolution at very high temperatures of a nickel-based single crystal superalloy.* Metallurgical and Materials Transactions A, 2013. **44A**: p. 131-146.
94. J. Cormier and G. Cailletaud, *Constitutive modeling of the creep behavior of single crystal superalloys under non-isothermal conditions inducing phase transformations.* Materials Science and Engineering A, 2010. **527**(23): p. 6300-6312.
95. J. Cormier, X. Milhet, and J. Mendez, *Effect of very high temperature short exposures on the dissolution of the γ′ phase in single crystal MC2 superalloy.* Journal of Materials Science, 2007. **42**(18): p. 7780-7786.
96. J.-B. le Graverend, L. Dirand, A. Jacques, J. Cormier, O. Ferry, T. Schenk, F. Gallerneau, S. Kruch, and J. Mendez, *In situ measurement of the γ/γ' lattice mismatch evolution of a nickel-based single crystal superalloy during non-isothermal very high temperature creep experiments.* Metallurgical and Materials Transactions A, 2012. **43A**: p. 3946-3951.
97. M. Probst-Hein, A. Dlouhy, and G. Eggeler, *Dislocation interactions in γ -channels between γ′-particles of superalloy single crystals.* Material Science and Engineering, 2001. **A319-321**: p. 379-382.
98. A. Cervellon, J. Cormier, F. Mauget, and Z. Hervier, *VHCF life evolution after microstructure degradation of a Ni-based single crystal superalloy.* International Journal of Fatigue, 2017. **104**: p. 251-262.
99. R. Desmorat, A. Mattiello, and J. Cormier, *A tensorial thermodynamic framework to account for the γ′ rafting in Nickel-based single crystal superalloys.* International Journal of Plasticity, 2017. **95**: p. 43-81.
100. J.-B. le Graverend, J. Cormier, F. Gallerneau, P. Villechaise, S. Kruch, and J. Mendez, *A microstructure-sensitive constitutive modeling of the inelastic behavior of single*

crystal nickel based superalloys at very high temperature. International Journal of Plasticity, 2014. **59**: p. 55-83.
101. H.T. Pang, H.B. Dong, R. Beanland, H.J. Stone, C.M.F. Rae, P.A. Midgley, G. Brewster, and N. D'Souza, *Microstructure and solidification sequence of the interdendritic region in a third generation single-crystal nickel-base superalloy.* Metallurgical and Materials Transactions A, 2009. **30A**: p. 1660-1669.
102. G.E. Fuchs and B.A. Boutwell, *Calculating Solidification and Transformation in As-Cast CMSX-10.* JOM, 2002(January): p. 45-48.
103. B.C. Wilson, E.R. Cutler, and G.E. Fuchs, *Effect of solidification parameters on the microstructures and properties of CMSX-10.* Material Science and Engineering A, 2008. **A479**: p. 356-364.
104. B.C. Wilson, J.A. Hickman, and G.E. Fuchs, *The Effect of Solution Heat Treatment on a Single-Crystal Ni-Based Superalloy.* JOM, 2003. **55**(March 2003): p. 35-40.
105. Y. Zhang, L. Liu, T. Huang, Y. Li, Z. Jie, J. Zhang, W. Yang, and H. Fu, *Investigation on remelting solution heat treatment for nickel-based single crystal superalloys.* Scripta Materialia, 2017. **136**: p. 74-77.
106. P.D. Jablonski and C.J. Cowen, *Homogenizing a nickel-based superalloy: thermodynamic and kinetic simulation and experimental results.* Metallurgical and Materials Transactions B, 2009. **40**(2): p. 182-186.
107. M.S.A. Karunaratne, D.C. Cox, P. Carter, and R.C. Reed. *Modelling of the microsegregation in CMSX-4 superalloy and its homogenisation during heat treatment*. in *Superalloys 2000*. 2000. Seven Springs, PA, USA: TMS. p. 263-272.
108. C.E. Campbell, W.J. Boettinger, and U.R. Kattner, *Development of a diffusion mobility for Ni-base superalloys.* Acta Materialia, 2002. **50**: p. 775-792.
109. M.S.A. Karunaratne, P. Carter, and R.C. Reed, *Interdiffusion in the faced-centered cubic phase of the Ni-Re, Ni-Ta and Ni-W systems between 900 and 1300°C.* Material Science and Engineering, 2000. **A281**: p. 229-233.
110. A. Parsa, M. Ramsperger, A. Kostka, C. Somsen, C. Körner, and G. Eggeler, *Transmission electron microscopy of a CMSX-4 Ni-base superalloy produced by selective electron beam melting.* Metals, 2016. **6**(11): p. 258.
111. B. Ruttert, M. Ramsperger, L.M. Roncery, I. Lopez-Galilea, C. Körner, and W. Theisen, *Impact of hot isostatic pressing on microstructures of CMSX-4 Ni-base superalloy fabricated by selective electron beam melting.* Materials & Design, 2016. **110**: p. 720-727.
112. R. Rettig, N.C. Ritter, F. Müller, M.M. Franke, and R.F. Singer, *Optimization of the Homogenization Heat Treatment of Nickel-Based Superalloys Based on Phase-Field Simulations: Numerical Methods and Experimental Validation.* Metallurgical and Materials Transactions A, 2015. **46**(12): p. 5842-5855.
113. M. Cottura, Y. Le Bouar, B. Appolaire, and A. Finel, *Role of elastic inhomogeneity in the development of cuboidal microstructures in Ni-based superalloys.* Acta Materialia, 2015. **94**: p. 15-25.
114. B. Ruttert, O. Horst, I. Lopez-Galilea, D. Langenkämper, A. Kostka, C. Somsen, J. Goerler, M. Ali, O. Shchyglo, and I. Steinbach, *Rejuvenation of single-crystal Ni-base superalloy turbine blades: unlimited service life?* Metallurgical and Materials Transactions A, 2018. **49**(9): p. 4262-4273.
115. Y. Wang, D. Banerjee, C. Su, and A. Khachaturyan, *Field kinetic model and computer simulation of precipitation of L12 ordered intermetallics from fcc solid solution.* Acta Materialia, 1998. **46**(9): p. 2983-3001.
116. Y. Wen, B. Wang, J. Simmons, and Y. Wang, *A phase-field model for heat treatment applications in Ni-based alloys.* Acta Materialia, 2006. **54**(8): p. 2087-2099.

117. M. Fleck, F. Schleifer, M. Holzinger, and U. Glatzel, *Phase-Field Modeling of Precipitation Growth and Ripening During Industrial Heat Treatments in Ni-Base Superalloys.* Metallurgical and Materials Transactions A, 2018. **49**(9): p. 4146-4157.
118. I.M. Lifshitz and V.V. Slyozov, Journal of Physical Chemistry solids, 1961. **19**(1/2): p. 35-50.
119. C. Wagner, Zeitschrift für Elektrochemie, 1961. **65**(7/8): p. 581-591.
120. L. Rettberg, M. Tsunekane, and T. Pollock. *Rejuvenation of nickel-based superalloys GTD444 (DS) and RENE N5 (SX).* in *Superalloys 2012*. 2012. Seven Springs, PA, USA. p. 341-349.
121. B. Ruttert, D. Bürger, L.M. Roncery, A.B. Parsa, P. Wollgramm, G. Eggeler, and W. Theisen, *Rejuvenation of creep resistance of a Ni-base single-crystal superalloy by hot isostatic pressing.* Materials & Design, 2017. **134**: p. 418-425.
122. Z. Yao, C. Degnan, M. Jepson, and R. Thomson, *Effect of rejuvenation heat treatments on gamma prime distributions in a Ni based superalloy for power plant applications.* Materials Science and Technology, 2013. **29**(7): p. 775-780.
123. P.R. Bhowal, E.F. Wright, and E.L. Raymond, *Effects of cooling rate and γ′ morphology on creep and stress-rupture properties of a powder metallurgy superalloy.* Metallurgical Transactions A, 1990. **21**(6): p. 1709-1717.
124. A. Laurence, J. Cormier, P. Villechaise, T. Billot, J.-M. Franchet, F. Pettinari-Sturmel, M. Hantcherli, F. Mompiou, and A. Wessman. *Impact of the solution cooling rate and of thermal aging on the creep properties of the new cast & wrought René 65 Ni-based superalloys*. in *8th International Symposium on Superalloy 718 and Derivatives*. 2014. Pittsburgh, PA, USA: TMS. p. 333-348.
125. L. Thébaud, P. Villechaise, C. Crozet, A. Devaux, D. Béchet, J.-M. Franchet, A.-L. Rouffié, M.J. Mills, and J. Cormier, *Is there an optimal grain size for creep resistance in Ni-based disk superalloys?* Material Science & Engineering A, 2018. **716**: p. 274-283.
126. F. Cosentino, N. Warnken, J.-C. Gebelin, and R.C. Reed, *Numerical and experimental study of post-heat treatment gas quenching and its impact on microstructure and creep in CMSX-10 superalloy.* Journal of Materials Processing Technology, 2013. **213**(12): p. 2350-2360.
127. F. Cosentino, N. Warnken, J.-C. Gebelin, and R.C. Reed, *Numerical modeling of vacuum heat treatment of nickel-based superalloys.* Metallurgical and Materials Transactions A, 2013. **44**(11): p. 5154-5164.
128. R. Chieragatti and L. Rémy, *Influence of orientation on the low cycle fatigue of MAR-M 200 single crystals at 650°C. I: Fatigue life behaviour.* Materials Science and Engineering: A, 1991. **141**(1): p. 1-9.
129. D.W. MacLachlan and D.M. Knowles, *Fatigue behaviour and lifing of two single crystal superalloys.* Fatigue Fract Engng Mater Struct, 2001. **24**: p. 503-521.
130. C.L. Brundidge, *Development of a processing-structure-fatigue property model for single crystal superalloys*, PhD Thesis. 2011, University of Michigan.
131. C.L. Brundidge, J.D. Miller, and T.M. Pollock, *Development of Dendritic Structure in the Liquid-Metal-Cooled, Directional-Solidification Process.* Metallurgical and Materials Transactions A, 2011. **42**: p. 2723-2732.
132. A. Cervellon, J. Cormier, F. Mauget, Z. Hervier, and Y. Nadot, *Very high cycle fatigue of Ni-based single crystal superalloys at high temperature.* Metallurgical and Materials Transactions A, 2018. **49A**: p. 3938-3950.
133. A. Cervellon, *Propriétés en fatigue à grand et très grand nombre de cycles et à haute température des superalliages base nickel monogranulaires*, PhD thesis, in *Institut Pprime*. 2018, ISAE-ENSMA: Futuroscope-Chasseneuil.

134. W.-J. Zhang, *Thermal mechanical fatigue of single crystal superalloys: Achievements and challenges.* Materials Science and Engineering: A, 2016. **650**: p. 389-395.